

Scattering control of optical nano-antennas with designed excitations

Wei, Lei

DOI

[10.4233/uuid:5c991eac-9fca-4b85-af77-0de4d1e4a8ac](https://doi.org/10.4233/uuid:5c991eac-9fca-4b85-af77-0de4d1e4a8ac)

Publication date

2018

Document Version

Final published version

Citation (APA)

Wei, L. (2018). *Scattering control of optical nano-antennas with designed excitations*. [Dissertation (TU Delft), Delft University of Technology]. <https://doi.org/10.4233/uuid:5c991eac-9fca-4b85-af77-0de4d1e4a8ac>

Important note

To cite this publication, please use the final published version (if applicable).
Please check the document version above.

Copyright

Other than for strictly personal use, it is not permitted to download, forward or distribute the text or part of it, without the consent of the author(s) and/or copyright holder(s), unless the work is under an open content license such as Creative Commons.

Takedown policy

Please contact us and provide details if you believe this document breaches copyrights.
We will remove access to the work immediately and investigate your claim.

**SCATTERING CONTROL OF OPTICAL
NANO-ANTENNAS WITH DESIGNED EXCITATIONS**

SCATTERING CONTROL OF OPTICAL NANO-ANTENNAS WITH DESIGNED EXCITATIONS

Proefschrift

ter verkrijging van de graad van doctor
aan de Technische Universiteit Delft,
op gezag van de Rector Magnificus Prof. dr. ir. T.H.J.J. van der Hagen,
voorzitter van het College voor Promoties,
in het openbaar te verdedigen op
dinsdag 25 september 2018 om 15:00 uur

door

Lei WEI

Master of Science, Applied Physics
Technische Universiteit Delft, Delft, Nederland,
geboren te Taihe county, Anhui province, P.R. China.

Dit proefschrift is goedgekeurd door de

promotor: prof. dr. H. P. Urbach

copromotor: dr. N. Bhattacharya

Samenstelling promotiecommissie:

Rector Magnificus,	voorzitter
Prof. dr. H. P. Urbach,	Technische Universiteit Delft
Dr. N. Bhattacharya,	Technische Universiteit Delft

Onafhankelijke leden:

Prof. dr. L. K. Kuipers	Technische Universiteit Delft
Prof. dr. A. P. Mosk	Universiteit Utrecht
Prof. dr. P. W. H. Pinkse	University of Twente
Dr. P. K. de Bokx	Philips Innovation Labs
Prof. dr. W. M. J. Coene	ASML
Prof. dr. B. Rieger,	Technische Universiteit Delft, reservelid



This thesis is supported by NanoNextNL, a micro and nanotechnology innovation consortium of the Government of the Netherlands and 130 partners from academia and industry.

Keywords: Nano-antenna, Mie theory, vector vortex beam, non-radiating current source, directional scattering

Copyright © 2018 by L.Weï

ISBN 978-94-028-1148-3

An electronic version of this dissertation is available at
<http://repository.tudelft.nl/>.

This thesis is dedicated to my parents.

CONTENTS

Summary	ix
Samenvatting	xi
1 Introduction	1
References	5
2 Shaping the focal field of vector vortex beams	9
2.1 Introduction	10
2.2 Vectorial Debye diffraction integral	10
2.3 Focal field of azimuthally and radially polarized Zernike polynomials	13
2.4 Focal field shaping	17
2.4.1 Longitudinally polarized elongated subwavelength hollow channel	19
2.4.2 On-axis circularly polarized focal field	19
2.4.3 On-axis multiple circularly polarized focal spots	21
2.5 Discussions	23
2.6 Conclusion	24
References	26
3 Excitation of the radiationless anapole mode	29
3.1 Introduction	30
3.2 Single beam excitation	30
3.3 "ideal" radiationless anapole excitation under 4π configuration	33
3.4 Conclusion	35
References	37
4 Adding a spin to Kerker's condition: angular tuning of directional scattering with designed excitation	39
4.1 Introduction	40
4.2 Basic physical model	40
4.3 Designed excitation with focused vector vortex beams	42
4.4 Numerical verifications	44
4.5 Conclusion	47
References	48
5 Suspended nano-antenna array	51
5.1 Introduction	52
5.2 Floating nano-antenna array and silicon substrate	52
5.3 Suspended nano-antenna array	54
5.4 Nano-fabrication of the suspended nano-antenna array	60
5.5 Conclusion	60

References	62
6 Outlook	65
References	68
Acknowledgements	69
Curriculum Vitae	1
List of Publications	3

SUMMARY

In this thesis, we start with investigating the unique focusing properties of vector vortex beams which possess structured polarizations, amplitudes and phases. We show that the focal fields can be shaped with desired polarization and intensity distributions by engineering the pupil fields with radially or azimuthally polarized Zernike polynomials. The shaped focal field is of importance for optimizing optical trapping and improving the resolution of optical microscopes as a structured illumination beam. The polarization topologies at the focus of structured vector beams can be used to determine the orientations of the molecule dipole moment in order to achieve ultimate positioning precision. What's more interesting may be the interaction of the shaped focal fields with structured nano-objects, which offers nice opportunities not only to test some of the fundamental physics but also to propose novel concepts that potentially lead to applications. This is evidenced by the two major results of this thesis in chapter 3 and chapter 4, where both use focused vector vortex beams as designed excitations to control the scattering of a high index dielectric nano-sphere.

In chapter 3, we studied a relative fundamental problem—the existence of non-radiating current sources, which was treated extensively in the inverse problems since 1970s yet a practical demonstration is still lacking. We propose for the first time a method for the excitation of an ‘ideal’ anapole, a current source induced inside the dielectric nanosphere by external excitation yet remains radiationless due to the complete destructive interference of the current toroidal dipole and electric dipole moments. The proposed excitation configuration is composed of two counter-propagating focused radially polarized beams under 4π configuration, with exactly the same amplitude distribution but π phase difference. We show such illumination enables pure excitation of an anapole without violating the reciprocity theorem.

While in chapter 4, we proposed a novel concept to control the directional scattering of light. By adding a spin to one of the linear electric and magnetic dipoles whose interference defines the conventional Kerker's condition for directional scattering, we introduce a new degree of freedom, i.e. angular tuning of unidirectional scattering. We further demonstrate that arbitrary angular tuning over a broad wavelength range is possible, by independently exciting and controlling a longitudinal electric and a spinning magnetic dipole mode of a high index dielectric nanosphere with designed focal fields. This result has implications in any application that requires directional light routing.

At the last part of this thesis, we study the properties of plasmonic nano-antenna arrays with the ultimate goal for improving the infrared spectroscopy. We find out that suspended nano-antenna arrays supported by Si nanopillars outperform those with direct contact on substrates considerably in terms of field enhancement. The field enhancement is strongly dependent on the height of the suspended nano-antenna array. In order to achieve the best enhancement, an optimum height has to be achieved. Additionally, the resonant frequencies are also tunable with incidence angle. A recipe is developed for

the fabrication of such suspended nano-antenna array. The work in this chapter forms both design and fabrication guidelines for future researches applying these structured nano-antenna arrays in surface enhanced infrared spectroscopy.

SAMENVATTING

In dit proefschrift beginnen we met het onderzoeken van de unieke focus eigenschappen van vector vortex lichtbundels die gestructureerde polarisaties, amplitudes en fasen bezitten. We laten zien dat het veld in het brandpunt kan gevormd worden met gewenste polarisatie- en intensiteitsverdelingen door de pupilvelden te ontwerpen met radiaal en azimutaal gepolariseerde Zernike-polynomen. Het gevormde brandpuntveld is van belang voor het optimaliseren van optische trapping en het verbeteren van de resolutie van optische microscopen als een gestructureerde verlichtingsbundel. De polarisatie topologieën in het brandpunt van gestructureerde vector lichtbundels kunnen gebruikt worden om de oriëntaties van het molecuuldipoolmoment te bepalen om de ultieme positioneringsprecisie te bereiken.

Wat interessant is, is de interactie tussen de gevormde brandpunten met gestructureerde nano-objecten, die mooie kansen bieden om niet alleen fundamentele fysica te testen, maar ook nieuwe concepten voor te stellen die potentieel tot toepassingen leiden. Dit blijkt uit de twee hoofdresultaten van dit proefschrift in hoofdstuk 3 en hoofdstuk 4, waarbij beide resultaten gebruik maken van gefocusseerde vector vortex lichtbundels als ontworpen excitaties om de verstrooiing van een hoge-index diëlektrische nanobol te controleren.

In hoofdstuk 3 hebben we een relatief fundamenteel probleem bestudeerd: het bestaan van stralingloze stroombronnen, dat sinds de jaren zeventig uitgebreid in de inverse problemen is behandeld, maar een praktische demonstratie ontbreekt nog steeds. We stellen voor het eerst een methode voor de excitatie van een 'ideale' anapool voor, een stroombron die door de externe excitatie in de diëlektrische nanosfeer wordt geïnduceerd, blijft stralingloos door de volledige destructieve interferentie van de stroom toroidale dipool en elektrische dipoolmomenten. De voorgestelde excitatieconfiguratie bestaat uit twee radiaal gepolariseerde lichtbundels onder 4π configuratie, met precies dezelfde amplitudeverdeling maar π faseverschil. We laten zien dat dergelijke verlichting de pure excitatie van een anapole mogelijk maakt zonder de wederkerigheidstheorie te schenden.

In hoofdstuk 4 hebben we een nieuw concept voorgesteld om de directionele verstrooiing van het licht te beheersen. Door een spin toe te voegen aan een van de lineaire elektrische en magnetische dipolen waarvan de interferentie de traditionele Kerker's conditie voor directionele verstrooiing definieert, introduceren we een nieuwe vrijheidsgraad, namelijk hoekafstemming van unidirectionele verstrooiing. We tonen verder aan dat willekeurige hoekafstemming over een brede golflengtebereik mogelijk is, door een longitudinale elektrische en een draaiende magnetische dipoolmodus van een hoge-index-diëlektrische nanosfeer onafhankelijk te exciteren en te controleren met ontworpen brandpuntveld. Dit resultaat heeft implicaties in elke applicatie die directionele licht routing vereist.

In het laatste deel van dit proefschrift bestuderen we de eigenschappen van plasmoni-

sche nano-antenne arrays met het ultieme doel om de infrarood spectroscopie te verbeteren. We vinden dat nano-antenne arrays ondersteund door Si nanopilaren beter presteren dan die met direct contact op substraten, wat betreft veldversterking. De veldversterking is sterk afhankelijk van de hoogte van de nano-antenne array. Om de beste versterking te behalen, moet een optimale hoogte worden bereikt. Bovendien zijn de resonantiefrequenties ook af te stemmen met de invalshoek. Een recept is ontwikkeld voor de fabricage van een dergelijke nano-antenne array. Het werk in dit hoofdstuk vormt zowel ontwerp- en fabricage-richtlijnen voor toekomstige onderzoeken die deze gestructureerde nano-antenne-arrays toepassen in de infrarood spectroscopie.

1

INTRODUCTION

The investigation of light and matter interactions is at the heart of optical physics. One example is optical trapping [1] small objects with focused laser beams. Since the seminal works [2, 3] by Arthur Ashkin et al., optical trapping and manipulations remains an enabling technique for new discoveries to this day with applications ranging from optical trapping of atoms [4], tests of fundamental physics with levitated nanoparticles [5, 6], ultrasensitive force measurement [7] as well as applications in single molecule biophysics [8, 9].

In recent years, the study of the interaction of light and matter has been enriched by renewed focus due to the capability of precise generation of structured optical fields as well as structured materials [10–12]. With the development of spatial light modulators [12], meta-surfaces [13] and q-plates [14–16], arbitrary optical fields with spatially varying polarization, amplitude and phase can be generated. Examples are vector vortex beams [17] with high topological degree and tightly focused spots with optimum electric field component. This provides us with a new perspective in exploring the physics of structured light and matter interactions and unlocks new applications.

For instance, beams with phase singularities that carry orbital angular momentum (OAM) [18] lead to debates about the fundamental aspects of angular momentum in optical fields, which continue until today [19]. Yet such beams already find wide applications such as in super-resolution microscopy [20], optical tweezers [11], tele-communications [21] and quantum information [22], etc.

Another feature of vector vortex beams is structured polarization. By focusing structured polarized beams, complex polarization topologies in the focal region can be generated [23]. For instance, tightly focused radially polarized beam can generate a sharp longitudinal electric field which has been used to probe the dipole moment orientation of fluorescent molecules [24, 25], a parameter critical in achieving the ultimate precision limit of the super-resolution localization microscopes [20].

Apart from fluorescent molecules, there exist a large group of more general structured nano-objects including plasmonic nano-particles [26], high index dielectric nanoparticles [27] and core shell nanoparticles [28] that can be produced with desirable accuracy with modern nano-fabrication facilities and exhibit special spectral and scattering properties. The study of the interaction (scattering/radiation) of these structured nanoparticles with designed focused vector vortex beams is an important and interesting topic.

First of all, well characterized nanoparticles and focal fields together form an ideal platform for exploring some fundamental physical phenomenon. One interesting example is the recent pair of experimental demonstrations [29, 30] of Kerker's conditions on directional scattering at optical frequencies which was originally discussed in 1983 [31]. Secondly, the interaction between special fields and particles can be utilized in applications of precision metrology. The reconstruction of the local amplitude and phase of the tightly focused vector beam with unprecedented resolution is demonstrated recently based on the interference between the scattered field of a well characterized nanoparticle and incident beam [23, 32]. On the other hand, well characterized focal fields enable the detection and nanoscale localization [33–35] of nanoparticles. Last but not least, focusing vector vortex beams with designed multipole components [36, 37] can be used to selectively excite specific scattering modes of a nanoparticle [38, 39] and further shape the scattering pattern of the nanoparticle as an optical antenna based on the multipolar

interference effect [40].

In this dissertation, we deal with the following subjects:

1. In chapter 2, we study the focal field properties of radially/azimuthally polarized complex Zernike polynomials. Based on this knowledge, a pupil design method for the focal field shaping is introduced with the simplicity that only a handful of Zernike coefficients are needed in the optimization. With this method, we are able to obtain a pupil field to generate a longitudinally polarized hollow spot with a depth of focus up to 12λ and 0.28λ lateral resolution (FWHM) for an optical system with numerical aperture 0.99; A pupil field to generate 8 circularly polarized axial focal spots is also obtained.
2. In chapter 3, we study the excitation of radiationless anapole. The existence of non-radiating current sources such as the anapole is of fundamental importance for inverse scattering problems and designing of invisible objects. However, the excitation of such radiationless sources is quite challenging and its experimental demonstration was lacking until 2015 [41]. Yet, the excited anapole in [41] is not ideally radiationless because the magnetic quadrupole mode cannot be completely suppressed. We present a method based on which the anapole mode of a high index isotropic dielectric nanosphere can be excited but radiationless. We show that this radiationless anapole is attributed to the destructive interference of the Cartesian dipole moment and the toroidal dipole moment of the induced current by our proposed focused radially polarized beam illumination. Further, with a standing wave illumination formed by two counterpropagating focused radially polarized beams in a 4π configuration, the ideal radiationless anapole can be excited. This result illustrates a case where a radiationless mode is excited by external illumination but the reciprocity theorem is nevertheless not violated.
3. In chapter 4, we propose a concept to achieve arbitrary angular tuning of directional scattering over a relatively broad wavelength range. Precise control of the scattering by subwavelength nanostructures is becoming an important research topic with applications to the directional coupling of light into photonic chips. Among others, directional scattering of high index dielectric nanoparticles has been demonstrated recently at optical frequencies [29, 30]. The directionality originates from the interference of the linear electric and magnetic dipole modes of the dielectric nanoparticle under plane wave illumination, similar to Kerker's conditions for magneto-dielectric nanoparticles. However, the ideal directionality is limited to a single wavelength and forward direction where the wave propagates for a given dielectric nanoparticle. Starting from a simple physical model based on the a longitudinal electric dipole and a spinning magnetic dipole, we show that the directionality can be tuned to any direction within a selected plane by simply changing the relative phase of the dipoles. Furthermore, using the unique focusing properties of an azimuthally polarized phase vortex beam and a radially polarized beam, we propose an approach to simultaneously excite and independently control a spinning magnetic and a longitudinal electric dipole of a high index dielectric nanoparticle at the focal point. We show that by simply adjusting the phase and amplitude of the field on the exit pupil of the optical system, the scattering of

the nanosphere can be tuned to any direction within a plane and that the method works over a broad wavelength range.

4. In chapter 5, we have investigated the substrate effect on the plasmonic resonances and proposed a suspended nano-antenna array to enable large field enhancement with the ultimate goal to improve the performance of surface enhanced infrared spectroscopy. Specifically, we have studied the dependence of localized intensity enhancement on the height of the supporting Si pillars. It is shown that such suspended plasmonic nano-antenna array improve the field enhancement considerably compared to direct contact with the substrate. Further parameter optimization like adjust the pitch of the array can further improve the enhancement. A recipe for the fabrication of such nano-antenna array is also described.

REFERENCES

- [1] A. Ashkin, *History of optical trapping and manipulation of small-neutral particle, atoms, and molecules*, IEEE J. Selected Topics in Quantum Electronics **6**, 841 (2000).
- [2] A. Ashkin, *Acceleration and trapping of particles by radiation pressure*, Phys. Rev. Lett. **24**, 156 (1970).
- [3] A. Ashkin, *Observation of a single-beam gradient force optical trap for dielectric particles*, Optics Lett. **11**, 288 (1986).
- [4] S. Chu, J.E. Bjorkholm, A. Ashkin and A. Cable, *Experimental observation of optically trapped atoms*, Phys. Rev. Lett. **57**, 314 (1986).
- [5] S. Kheifets, S. Simha, K. Melin, T. Li and M.G. Raizen, *Observation of brownian motion in liquids at short times: instantaneous velocity and memory loss*, Science **343**, 1493 (2014).
- [6] V. Jain, J. Gieseler, C. Moritz, C. Dellago, R. Quidant and L. Novotny, *Direct measurement of photon recoil from a levitated nanoparticle*, Phys. Rev. Lett. **116**, 243601 (2016).
- [7] G. Ranjit, M. Cunningham, K. Casey and A.A. Geraci, *Zeptonewton force sensing with nanospheres in an optical lattice*, Phys. Rev. A **93**, 053801 (2016).
- [8] K.C. Neuman and A. Nagy, *Single-molecule force spectroscopy: optical tweezers, magnetic tweezers and atomic force microscopy*, Nature Methods **5**, 491 (2008).
- [9] M.D. Wang, H. Yin, R. Landick, J. Gelles and S.M. Block, *Stretching dna with optical tweezers*, Biophys. Journal **72**, 1335 (1997).
- [10] H. Rubinsztein-Dunlop, *Roadmap on structured light*, J. Optics **19**, 013001 (2016).
- [11] M. Padgett and R. Bowman, *Tweezers with a twist*, Nature Photonics **5**, 343 (2011).
- [12] M. Woerdemann, C. Alpmann, M. Esseling and C. Denz, *Advanced optical trapping by complex beam shaping*, Laser & Photonics Rev. **7**, 839 (2013).
- [13] F.Y. Yue, D.D. Wen et al., *Vector vortex beam generation with a single plasmonic metasurface*, ACS Photonics **3**, 1558 (2016).
- [14] V. D'Ambrosio, F. Baccari, et al., *Arbitrary, direct and deterministic manipulation of vector beams via electrically-tuned q-plates*, Scientific Reports **5** (2015).
- [15] Z. Liu, Y. Liu, et al., *Generation of arbitrary vector vortex beams on hybrid-order poincaré sphere*, Photonics Research **5**, 15 (2017).
- [16] D. Naidoo, E.S. Roux et al., *Controlled generation of higher-order poincaré sphere beams from a laser*, Nature Photonics **10**, 327 (2016).

- [17] G. Milione, H.I. Sztul, D.A. Nolan and R.R. Alfano, *Higher-order poincaré sphere, stokes parameters, and the angular momentum of light*, Phys. Rev. Lett. **107**, 053601 (2011).
- [18] L. Allen, M.W. Beijersbergen et al., *Orbital angular momentum of light and the transformation of laguerre-gaussian laser modes*, Phys. Rev. A **45**, 8185 (1992).
- [19] S.M. Barnett, L. Allen, R.P. Cameron, et al., *On the natures of the spin and orbital parts of optical angular momentum*, J. Opt. **18** (2016).
- [20] F. Balzarotti, Y. Eilers et al., *Nanometer resolution imaging and tracking of fluorescent molecules with minimal photon fluxes*, Science **355**, 606 (2017).
- [21] N. Bozinovic, Y. Yue et al., *Terabit-scale orbital angular momentum mode division multiplexing in fibers*, Science **340**, 1545 (2013).
- [22] G. Vallone, V. D'Ambrosio et al., *Free-space quantum key distribution by rotation-invariant twisted photons*, Phys. Rev. Lett. **113**, 060503 (2014).
- [23] T. Bauer, P. Banzer, E. Karimi et al., *Observation of optical polarization möbius strips*, Science **347**, 964 (2015).
- [24] T. Zuchner, A.V. Failla and A. J. Meixner, *Light microscopy with doughnut modes: a concept to detect, characterize, and manipulate individual nanoobjects*, Angewandte Chemie **50**, 5274 (2011).
- [25] L. Novotny, M.R. Beversluis, K.S. Youngworth and T.G. Brown, *Longitudinal field modes probed by single molecules*, Phys. Rev. Lett. **86**, 5251 (2001).
- [26] S.A. Maier and H.A. Atwater, *Plasmonics: Localization and guiding of electromagnetic energy in metal/dielectric structures*, J. Appl. Phys. **98**, 011101 (2005).
- [27] A. Kuznetsov, A.E. Miroshnichenko, M.L. Brongersma, Y.S. Kivshar and B. Luk'yanchuk, *Optically resonant dielectric nanostructures*, Science **354**, aag2472 (2016).
- [28] W. Liu, A.E. Miroshnichenko, D.N. Neshev and Y.S. Kivshar, *Broadband unidirectional scattering by magneto-electric core shell nanoparticles*, ACS NANO **6**, 5489 (2012).
- [29] S. Person, M. Jain, et al., *Demonstration of zero optical backscattering from single nanoparticles*, Nano Letters **13**, 1806 (2013).
- [30] Y.H. Fu, A.I. Kuznetsov, et al., *Directional visible light scattering by silicon nanoparticles*, Nature Comm. **4** (2013).
- [31] M. Kerker, D.S. Wang and C.L. Giles, *Electromagnetic scattering by magnetic spheres*, J. Opt. Soc. Am. **73**, 765 (1983).

- [32] T. Bauer, S. Orlov, U. Peschel, P. Banzer and G. Leuchs, *Nanointerferometric amplitude and phase reconstruction of tightly focused vector beams*, *Nature Photonics* **8**, 23 (2014).
- [33] S. Roy, et al., *Radially polarized light for detection and nanolocalization of dielectric particles on a planar substrate*, *Phys. Rev. Lett.* **114**, 103903 (2015).
- [34] M. Neugebauer, P. Wozniak, A. Bag, G. Leuchs and P. Banzer, *Polarization-controlled directional scattering for nanoscopic position sensing*, *Nature Comm.* **7**, 11286 (2016).
- [35] Z. Xi et al., *Accurate feeding of nanoantenna by singular optics for nanoscale translational and rotational displacement sensing*, *Phys. Rev. Lett.* **117**, 113903 (2016).
- [36] T.X. Hoang, X.D. Chen and C.J.R. Sheppard, *Multipole theory for tight focusing of polarized light, including radially polarized and other special cases*, *JOSA A* **29**, 32 (2012).
- [37] T.X. Hoang, X.D. Chen and C.J.R. Sheppard, *Interpretation of the scattering mechanism for particles in a focused beam*, *Phys. Rev. A* **86**, 033817 (2012).
- [38] P. Wozniak, P. Banzer and G. Leuchs, *Selective switching of individual multipole resonances in single dielectric nanoparticles*, *Laser & Photonics Rev.* **9**, 231 (2015).
- [39] T. Das, P.P. Iyer, R.A. DeCrescent and J.A. Schuller, *Beam engineering for selective and enhanced coupling to multipolar resonances*, *Phys. Rev. B* **92**, 241110 (2015).
- [40] W. Liu and Y.S. Kivshar, *Multipolar interference effects in nanophotonics*, *Phil. Trans. R. Soc. A* **375**, 20160317 (2017).
- [41] A.E. Miroshnichenko, et al., *Nonradiating anapole modes in dielectric nanoparticles*, *Nature Comm.* **6** (2015).

2

SHAPING THE FOCAL FIELD OF VECTOR VORTEX BEAMS

The focal field properties of radially and azimuthally polarized Zernike polynomials are studied. A method to design the pupil field in order to shape the focal field of radially or azimuthally polarized phase vortex is introduced. With this method, we are able to obtain a pupil field to achieve a longitudinally polarized hollow spot with a depth of focus up to 12λ and 0.28λ lateral resolution (FWHM) for a optical system with numerical aperture 0.99; A pupil field to generate 8 focal spots along the optical axis is also obtained with this method.

2.1. INTRODUCTION

Focal field shaping by engineering the polarization, amplitude and phase on the exit pupil of an optical system [2–4], especially with the help of spatial light modulators [5–7] and q-plates [8–10], has attracted a lot of attention in recent years. Optial focal field shaping has many applications. For instance, a beam with a phase vortex or azimuthal polarization on the exit pupil can generate a hollow focus [11, 12], with zero intensity in the center. Such a hollow focus can be used to trap absorbing particles, cold atoms [13] and can also be applied in high resolution STED microscopy [14]. The ability to control the local electric and magnetic field distribution in the focal region makes it possible to determine the orientation of a single optical emitter [15] or excite certain resonances of a quantum emitter [16] which is not possible otherwise. Tight focusing behavior of polarized phase vortex beams [17, 18] has been investigated to achieve sharp resolution [19, 20], and to demonstrate spin-to-orbital angular momentum conversion [21].

There are various methods to design a structured radially or azimuthally polarized pupil, including binary phase masks [22] or reversing the electrical dipole array radiation at the focus [23–25]. Zernike polynomials form a complete and orthogonal set of polynomials on the unit circle, which form an ideal set to study the pupil engineering of circularly apertured optical imaging system. By precalculating the focal fields of Zernike polynomials, we can optimise the focal field by only optimising the Zernike coefficients. In this chapter, we first study the focal field properties of radially and azimuthally polarized Zernike polynomials. Based on this, we apply the pupil engineering method using complex Zernike polynomials to shape the focal field of a phase vortex beam with radial and azimuthal polarizations to generate an longitudinally polarized axially uniform hollow focus, a transversally polarized elongated spot, and multiple circularly polarized focal spots.

2.2. VECTORIAL DEBYE DIFFRACTION INTEGRAL

Consider an incoming beam that is propagating parallel to the optical axis and is focused by a high NA optical system as shown in Fig. 2.1. Without loss of generality, we consider the optical system is placed in vacuum so that the refractive index is $n=1$ in both object and image space. For a diffraction limited system the focal spot is the ideal image point as the center of the gaussian reference sphere. We assume the sine condition to be satisfied. This implies that when an incident ray which is parallel to the optical axis is extended and the corresponding focused ray is backwards extended, their point of intersection is on the gaussian reference sphere with radius R . In this session we will first derive the scalar Debye diffraction integral and then take the rotation of polarisation into account. This then leads to the vectorial Debye diffraction integral which has been discussed in Ref. [26–28].

Let (x_s, y_s) be a point on the exit pupil and let $E_s(x_s, y_s)$ be the electric field in this point of the incident beam that propagates parallel to the optical axis. This ray intersects with the corresponding focused ray in the point $P(x_s, y_s, \sqrt{R - x_s^2 - y_s^2})$ on the gaussian reference sphere as illustrated in Fig. 2.1. Based on the conservation of energy flux [27], it is

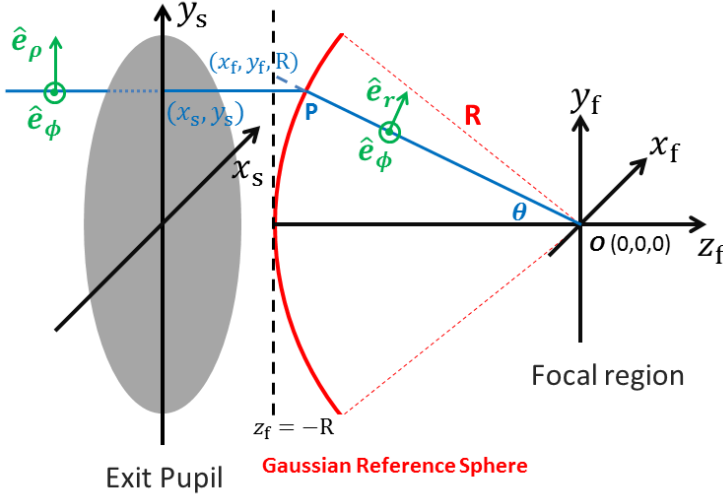


Figure 2.1: The Debye diffraction model. The gaussian reference sphere is centered at the geometrical focal spot O and the radius R is equal to the focal length. The focal coordinate is (x_f, y_f, z_f) with the geometrical focal point as its origin. The point P on the gaussian reference sphere is the intersection point of the incident ray which passes through the point (x_s, y_s) on the exit pupil and the corresponding focused ray OP . The field in the point $(x_f, y_f, -R)$ in the tangent plane $z_f = -R$ is obtained from that in P by back propagation of the converging spherical wave.

easy to prove that the field in the point P :

$$E_f(x_s, y_s, \sqrt{R - x_s^2 - y_s^2}) = E_s(x_s, y_s) \sqrt{\cos \theta} = E_s(x_s, y_s) \frac{(R - x_s^2 - y_s^2)^{1/4}}{\sqrt{R}}. \quad (2.1)$$

We use the angular spectrum representation to compute the field in the focal region. We first determine the electric field on the plane $z_f = -R$ as then compute its Fourier transform to determine the plane wave amplitude. We assume that the fields on the gaussian reference sphere is a spherical wave that converges to the gaussian focal point O . This assumption applies also to the case that the field on the gaussian reference sphere varies with position over the sphere as long as this variation is slow. The field in the point $(x_f, y_f, -R)$ on the plane $z_f = -R$ is calculated by back-propagating the field in the point $P(x_s, y_s, \sqrt{R - x_s^2 - y_s^2})$ on the gaussian reference sphere:

$$\begin{aligned} E_f(x_f, y_f, -R) &= E_f(x_s, y_s, \sqrt{R - x_s^2 - y_s^2}) \frac{R}{\sqrt{x_f^2 + y_f^2 + R^2}} e^{-ik(\sqrt{x_f^2 + y_f^2 + R^2} - R)} \\ &= E_s \left(\frac{R x_f}{\sqrt{x_f^2 + y_f^2 + R^2}}, \frac{R y_f}{\sqrt{x_f^2 + y_f^2 + R^2}} \right) \frac{R^{3/2}}{(x_f^2 + y_f^2 + R^2)^{3/4}} e^{-ik(\sqrt{x_f^2 + y_f^2 + R^2} - R)}, \end{aligned} \quad (2.2)$$

where the relations $x_s = \frac{Rx_f}{\sqrt{x_f^2 + y_f^2 + R^2}}$ and $y_s = \frac{Ry_f}{\sqrt{x_f^2 + y_f^2 + R^2}}$ are used.

The plane wave amplitudes are obtained by the Fourier transformation of the field in the plane $z_f = -R$:

$$\begin{aligned} \mathcal{F}(E_f) \left(\frac{k_x}{2\pi}, \frac{k_y}{2\pi}, -R \right) &= \iint E_f(x_f, y_f, -R) e^{-i(k_x x_f + k_y y_f)} dx_f dy_f \\ &= \iint E_s \left(\frac{Rx_f}{\sqrt{x_f^2 + y_f^2 + R^2}}, \frac{Ry_f}{\sqrt{x_f^2 + y_f^2 + R^2}} \right) \frac{R^{3/2}}{(x_f^2 + y_f^2 + R^2)^{3/4}} \\ &\quad \times e^{-ik(\sqrt{x_f^2 + y_f^2 + R^2} - R)} e^{-i(k_x x_f + k_y y_f)} dx_f dy_f. \end{aligned} \quad (2.3)$$

The asymptotic behavior of the double integral as $kR \gg 1$ can be evaluated by the method of stationary phase. A detailed outline of this method can be found in chapter 3.3 of Ref. [29]. The point of stationary phase in Eq. 2.3 is

$$x_f = -\frac{k_x}{k_z} R, \quad y_f = -\frac{k_y}{k_z} R, \quad (2.4)$$

where $k_z = \sqrt{k^2 - k_x^2 - k_y^2}$. Using the method of stationary phase, we have at this point:

$$\mathcal{F}(E_f) \left(\frac{k_x}{2\pi}, \frac{k_y}{2\pi}, -R \right) = -2\pi i E_s \left(-\frac{k_x}{k_z} R, -\frac{k_y}{k_z} R \right) \frac{R}{\sqrt{k k_z}} e^{-ik_z R}, \quad (2.5)$$

where $x_s = -\frac{k_x}{k} R$, $y_s = -\frac{k_y}{k} R$ and the constant term e^{ikR} is neglected. The plane wave amplitudes of the field on the focal plane $z_f = 0$ are obtained by multiplying Eq. 2.5 by $e^{ik_z R}$:

$$\mathcal{F}(E_f) \left(\frac{k_x}{2\pi}, \frac{k_y}{2\pi}, 0 \right) = -2\pi i E_s \left(-\frac{k_x}{k} R, -\frac{k_y}{k} R \right) \frac{R}{\sqrt{k k_z}}. \quad (2.6)$$

With the plane wave amplitudes known in Eq. 2.6, the field in the focal region can be calculated by the angular spectrum representation:

$$\begin{aligned} E_f(x_f, y_f, z_f) &= \frac{1}{4\pi^2} \iint_{\Omega} \mathcal{F}(E_f) \left(\frac{k_x}{2\pi}, \frac{k_y}{2\pi}, 0 \right) e^{i(k_x x_f + k_y y_f + k_z z_f)} dk_x dk_y \\ &= -\frac{iR}{2\pi} \iint_{\Omega} E_s \left(-\frac{k_x}{k} R, -\frac{k_y}{k} R \right) \frac{e^{ik_z z_f}}{\sqrt{k k_z}} e^{i(k_x x_f + k_y y_f)} dk_x dk_y \\ &= -\frac{iR}{2\pi} \iint_{\Omega} E_s \left(\frac{k_x}{k} R, \frac{k_y}{k} R \right) \frac{e^{ik_z z_f}}{\sqrt{k k_z}} e^{-i(k_x x_f + k_y y_f)} dk_x dk_y, \end{aligned} \quad (2.7)$$

The integration area in Eq. 2.7 is

$$\Omega = \{(k_x, k_y) : k_x^2 + k_y^2 \leq k_0^2 \text{NA}^2\}, \quad (2.8)$$

where the numerical aperture is $\text{NA} = na/R = n \sin \theta_{\max} = n s_0$ and a is the radius of the aperture of the exit pupil. Eq. 2.7 is also named the scalar Debye diffraction integral.

The polarisation of the electric field of the incoming ray in the point (x_s, y_s) on the exit pupil is rotated at the corresponding focused ray in the high NA optical system as illustrated in Fig. 2.1. Let (ρ, ϕ) be the normalised exit pupil coordinate:

$$x_s = a\rho \cos \phi, \quad y_s = a\rho \sin \phi, \quad (2.9)$$

A polarized pupil field can be written as a linear combination of the radially and azimuthally polarized parts. For a radially polarized incoming beam which propagates parallel to the optical axis, the ray in the point (x_s, y_s) on the exit pupil has a polarisation unit vector of the electric field

$$\hat{e}_s(\rho, \phi) = \hat{e}_\rho(\rho, \phi) = (\cos \phi, \sin \phi). \quad (2.10)$$

After the focusing lens, the polarisation of its corresponding focused ray is parallel to

$$\hat{e}_f(\theta, \phi) = (\cos \phi \cos \theta, \sin \phi \cos \theta, \sin \theta), \quad (2.11)$$

where (θ, ϕ) is the spherical coordinate that defines the focused ray and $\sin \theta = a\rho/R$. For an azimuthally polarized incoming beam which propagates parallel to the optical axis, the ray in the point (x_s, y_s) on the exit pupil has a polarisation unit vector of the electric field

$$\hat{e}_s(\rho, \phi) = \hat{e}_\phi(\rho, \phi) = (-\sin \phi, \cos \phi). \quad (2.12)$$

After the focusing lens, the polarisation of its corresponding focused ray is parallel to

$$\hat{e}_f(\theta, \phi) = (-\sin \phi, \cos \phi, 0). \quad (2.13)$$

Consider the pupil field $\mathbf{E}_s(\rho, \phi) = \hat{e}_s(\rho, \phi)E_s(\rho, \phi)$ is either radially or azimuthally polarized, the field in the focal region can then be calculated by the vectorial Debye-Wolf diffraction integral:

$$\mathbf{E}_f(x_f, y_f, z_f) = -\frac{iR}{2\pi} \iint_{\Omega} \hat{e}_f(\theta, \phi) E_s\left(\frac{k_x}{k}R, \frac{k_y}{k}R\right) \frac{e^{ik_z z_f}}{\sqrt{k k_z}} e^{-i(k_x x_f + k_y y_f)} dk_x dk_y, \quad (2.14)$$

where we have the relation that

$$\sin \theta = a\rho/R = \frac{a}{R} \sqrt{\left(\frac{k_x}{k}\right)^2 + \left(\frac{k_y}{k}\right)^2}. \quad (2.15)$$

For a radially polarized pupil field, we apply $\hat{e}_f(\theta, \phi) = (\cos \phi \cos \theta, \sin \phi \cos \theta, \sin \theta)$ in Eq. 2.14, and for an azimuthally polarized pupil field, $\hat{e}_f(\theta, \phi) = (-\sin \phi, \cos \phi, 0)$ is applied.

2.3. FOCAL FIELD OF AZIMUTHALLY AND RADially POLARIZED ZERNIKE POLYNOMIALS

The complex Zernike polynomials $Z_n^m(\rho, \phi)$ form a complete set of orthogonal polynomials defined on the unit disc:

$$Z_n^m(\rho, \phi) = R_n^{|m|}(\rho) e^{im\phi}, \quad (2.16)$$

$$R_n^m(\rho) = \sum_{s=0}^p \frac{(-1)^s (n-s)!}{s!(q-s)!(p-s)!} \rho^{n-2s}, \quad (2.17)$$

where $p = \frac{1}{2}(n - |m|)$, $q = \frac{1}{2}(n + |m|)$, $n - |m| \geq 0$ and even, and (ρ, ϕ) is the normalised polar coordinate on the exit pupil plane. It is important to keep in mind that the complex Zernike polynomial defined here differs from the conventional Zernike polynomial used to analyze the phase aberrations, which is defined to be real. As we can see from its definition, Z_n^m has a phase singularity at $\rho = 0$ with the topological charge m .

The polarized electric field distribution on the exit pupil plane can be decomposed into a series of radially or azimuthally polarized Zernike polynomials:

$$\mathbf{E}_s(\rho, \phi) = \sum_{n,m} \hat{e}_s(\rho, \phi) \beta_n^m Z_n^m(\rho, \phi). \quad (2.18)$$

The electric field is polarized parallel the exit pupil plane, *i.e.* its z components vanishes. For a radially polarized pupil, the electric field is polarized along the radial direction of the unit circle $\hat{e}_s(\rho, \phi) = \hat{e}_\rho(\rho, \phi) = (\cos \phi, \sin \phi)$, while for azimuthal polarization, the electric field is polarized perpendicular to the radial direction of the unit circle $\hat{e}_s(\rho, \phi) = \hat{e}_\phi(\rho, \phi) = (-\sin \phi, \cos \phi)$.

The Zernike polynomials are very useful to analyze the aberrations of an optical system and have been used as a set of basis functions in the Extended Nijboer Zernike theory, where a semi-analytical solution of the focal field of each Zernike polynomial on the exit pupil is derived [30, 31].

The focusing properties of a field distribution on the exit pupil of a high NA optical system can be treated by the vectorial Debye diffraction integral [26]. In this chapter, we compute the focal fields of a pupil field that is decomposed into a summation of either radially polarized or azimuthally polarized Zernike polynomials defined in Eq. 2.18 in all points of the pupil. We numerically compute the vectorial Debye diffraction integral with a fast Fourier transform (FFT) method [32].

$$\begin{aligned} \mathbf{E}_f(x_f, y_f, z_f) &= -\frac{iR}{2\pi} \iint_{\Omega} \hat{e}_f(\theta, \phi) \sum_{n,m} \beta_n^m Z_n^m(\rho, \phi) \frac{e^{ik_z z}}{\sqrt{k k_z}} \exp[-i(k_x x_f + k_y y_f)] dk_x dk_y \\ &= \sum_{n,m} \beta_n^m \times \left\{ -\frac{iR}{2\pi} \iint_{\Omega} \hat{e}_f(\theta, \phi) Z_n^m(\rho, \phi) \frac{e^{ik_z z} \sqrt{\cos \theta}}{k_z} \exp[-i(k_x x_f + k_y y_f)] dk_x dk_y \right\} \end{aligned} \quad (2.19)$$

where R is the focal length, $k_z = \sqrt{k_0^2 n^2 - k_x^2 - k_y^2}$, $k_0 = 2\pi/\lambda$, and (x_f, y_f, z_f) is a point in the focal region, with geometrical focal point as origin. The integration area Ω is

$$\{(k_x, k_y) : k_x^2 + k_y^2 \leq k_0^2 \text{NA}^2\}, \quad (2.20)$$

where the numerical aperture is $\text{NA} = n \sin \theta_{\max} = n s_0$. $\hat{e}_f(\theta, \phi)$ is the unit vector that specifies the polarization of the electric field of the focusing ray defined by the angles θ and ϕ and we have the relation that

$$\sin \theta = a\rho/R = \frac{a}{R} \sqrt{\left(\frac{k_x}{k}\right)^2 + \left(\frac{k_y}{k}\right)^2}. \quad (2.21)$$

For a radially polarized pupil field, we apply $\hat{e}_f(\theta, \phi) = (\cos \phi \cos \theta, \sin \phi \cos \theta, \sin \theta)$ in Eq. 2.22, while for an azimuthally polarized pupil field, we use $\hat{e}_f(\theta, \phi) = (-\sin \phi, \cos \phi, 0)$. The focal field of a single radially or azimuthally polarized Zernike polynomials is:

$$\mathbf{E}_f^{nm}(x_f, y_f, z_f) = -\frac{iR}{2\pi} \iint_{\Omega} \hat{e}_f(\theta, \phi) Z_n^m(\rho, \phi) \frac{\sqrt{\cos \theta} e^{ik_z z}}{k_z} \exp[-i(k_x x_f + k_y y_f)] dk_x dk_y \quad (2.22)$$

Since the vectorial Debye diffraction integral depends linearly on the pupil field \mathbf{E}_s , the focal fields can be expressed by summation of the focal fields of each complex Zernike mode \mathbf{E}_f^{nm} with the same set of Zernike coefficients β_n^m as occur in the expansion of the pupil field:

$$\mathbf{E}_f(x_f, y_f, z_f) = \sum_{n,m} \beta_n^m \mathbf{E}_f^{nm}(x_f, y_f, z_f), \quad (2.23)$$

Once a set of coefficients β_n^m for \mathbf{E}_f^{nm} is found to give a desired focal distribution, the pupil field that gives this focal distribution can be obtained from Eq. 2.18.

In order to gain more insight into the focal fields of radially and azimuthally polarized Zernike polynomial, we rewrite Eq. 2.22 using polar coordinates:

$$\begin{aligned} \mathbf{E}_f^{nm}(\rho_f, \phi_f, z_f) = & -\frac{iR s_0^2}{\lambda} \int_0^1 (1 - \rho^2 s_0^2)^{-1/4} e^{ik_0 n z_f \sqrt{1 - \rho^2 s_0^2}} \\ & \times R_n^{|m|}(\rho) \rho d\rho \int_0^{2\pi} \hat{e}_f(\rho, \phi) e^{im\phi} e^{-i2\pi\rho\rho_f \cos(\phi_f - \phi)} d\phi, \end{aligned} \quad (2.24)$$

where, (ρ_f, ϕ_f, z_f) is the normalised cylindrical coordinate in the focal region, $\rho_f = \frac{n s_0}{\lambda} \sqrt{x_f^2 + y_f^2}$ and $s_0 = \sin \theta_{\max}$. For a radially polarized pupil field, we have $\hat{e}_f(\rho, \phi) = (\cos \phi \cos \theta, \sin \phi \cos \theta, \sin \theta)$, while for an azimuthally polarized pupil field, we have $\hat{e}_f(\rho, \phi) = (-\sin \phi, \cos \phi, 0)$.

The integral over azimuthal angle ϕ can be computed analytically following that $\int_0^{2\pi} e^{im\phi} e^{ix \cos(\phi - \phi')} d\phi = 2\pi i^m J_m(x) e^{im\phi'}$. The focal electric field components of the radially polarized pupil field are given by:

$$\begin{aligned} E_{f,x}^{nm}(\rho_f, \phi_f, z_f) = & -\frac{i\pi R s_0^2}{\lambda} i^{m+1} e^{im\phi_f} \int_0^1 \rho d\rho \\ & \times (1 - \rho^2 s_0^2)^{1/4} e^{ik_0 n z_f \sqrt{1 - \rho^2 s_0^2}} R_n^{|m|}(\rho) \\ & \times [e^{i\phi_f} J_{m+1}(2\pi\rho\rho_f) - e^{-i\phi_f} J_{m-1}(2\pi\rho\rho_f)], \end{aligned} \quad (2.25)$$

$$\begin{aligned} E_{f,y}^{nm}(\rho_f, \phi_f, z_f) = & -\frac{i\pi R s_0^2}{\lambda} i^m e^{im\phi_f} \int_0^1 \rho d\rho \\ & \times (1 - \rho^2 s_0^2)^{1/4} e^{ik_0 n z_f \sqrt{1 - \rho^2 s_0^2}} R_n^{|m|}(\rho) \\ & \times [e^{i\phi_f} J_{m+1}(2\pi\rho\rho_f) + e^{-i\phi_f} J_{m-1}(2\pi\rho\rho_f)], \end{aligned} \quad (2.26)$$

$$E_{f,z}^{nm}(\rho_f, \phi_f, z_f) = -\frac{i2\pi R s_0^2}{\lambda} i^m e^{im\phi_f} \int_0^1 \frac{s_0 \rho}{(1 - \rho^2 s_0^2)^{1/4}} \times e^{ik_0 n z_f \sqrt{1 - \rho^2 s_0^2}} R_n^{|m|}(\rho) J_m(2\pi \rho \rho_f) \rho d\rho. \quad (2.27)$$

2

From these equations, we can see that the focal field of a radially polarized phase vortex beam of topological charge m has the following properties:

1. Its transverse focal field components are proportional to $(1 - \rho^2 s_0^2)^{1/4}$, while its longitudinal component is proportional to $s_0 \rho / (1 - \rho^2 s_0^2)^{1/4}$. This means that for pupil fields with lower NA where the lower spatial frequencies dominate, the transverse components are stronger, while for a pupil function with higher NA where the higher spatial frequencies dominate, the longitudinal component is stronger. This gives a way to modulate the polarization in the focal region.
2. The transverse focal field components of the radially polarized pupil field $Z_n^{\pm 1}$ is non-zero and circularly polarized on the optical axis, due to the existence of J_0 in the integral.

As shown in Fig. 2.2(a), the radial polynomial $R_n^{|m|}$ modifies the focal field distribution in such a way that for a fixed m and $n > |m|$, the normalised $|E_z|^2$ has two maxima symmetrically distributed to the focal plane $z_f = 0$. As n increases, the separation between these two maxima along the z directions increases. From Fig. 2.2(b), we can see that the width of the longitudinal component $|E_z|^2$ of the focal field generated by radially polarized Z_n^m increases with increasing $|m| \neq 0$.

Similarly, the focal electric field of an azimuthally polarized pupil field can be written as:

$$E_{f,x}^{nm}(\rho_f, \phi_f, z_f) = \frac{i\pi R s_0^2}{\lambda} i^m e^{im\phi_f} \int_0^1 \rho d\rho \times (1 - \rho^2 s_0^2)^{-1/4} e^{ik_0 n z_f \sqrt{1 - \rho^2 s_0^2}} R_n^{|m|}(\rho) \times [e^{i\phi_f} J_{m+1}(2\pi \rho \rho_f) + e^{-i\phi_f} J_{m-1}(2\pi \rho \rho_f)], \quad (2.28)$$

$$E_{f,y}^{nm}(\rho_f, \phi_f, z_f) = -\frac{i\pi R s_0^2}{\lambda} i^{m+1} e^{im\phi_f} \int_0^1 \rho d\rho \times (1 - \rho^2 s_0^2)^{-1/4} e^{ik_0 n z_f \sqrt{1 - \rho^2 s_0^2}} R_n^{|m|}(\rho) \times [e^{i\phi_f} J_{m+1}(2\pi \rho \rho_f) - e^{-i\phi_f} J_{m-1}(2\pi \rho \rho_f)], \quad (2.29)$$

$$E_{f,z}^{nm}(\rho_f, \phi_f, z_f) = 0. \quad (2.30)$$

The focal field of an azimuthally polarized phase vortex of topological charge m has the following properties:

1. The polarization state of the electric field is kept in the focal region for the azimuthally polarized pupil field Z_n^0 , which can be easily derived from Eq. 2.28 and Eq. 2.29;

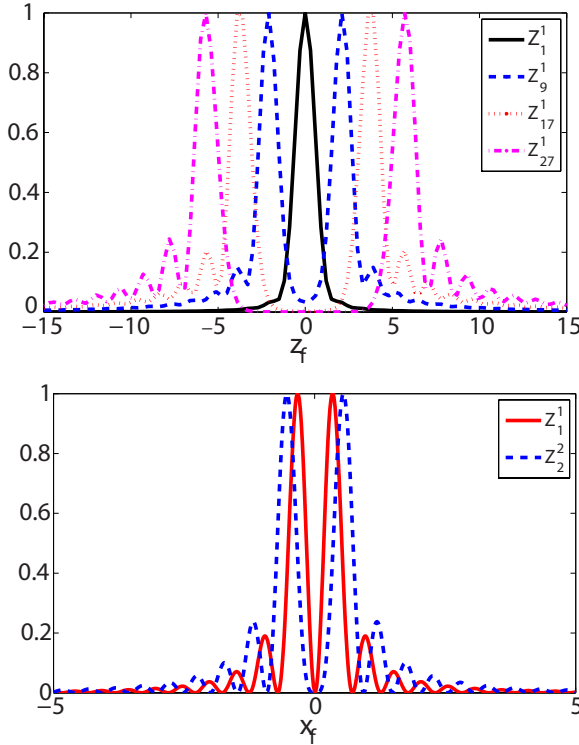


Figure 2.2: (a). Normalised $|E_z|^2$ for various radially polarized Z_n^1 along z_f direction, where the polar position ρ_f of $|E_z|^2$ is chosen that $|E_z|^2$ of each axial location is also at its maximum in the transverse plane. The numerical aperture s_0 is 0.99. (b). Normalised $|E_z|^2$ for various radially polarized pupil field Z_m^m along x_f axis, where the axial position ρ_f of $|E_z|^2$ is chosen that $|E_z|^2$ is its maximum in the $x_f - z_f$ plane. The numerical aperture s_0 is 0.99. (coordinates are in unit of incident light's wavelenth).

- From Eq. 2.28 and Eq. 2.29, it is easy to see that the transverse focal field components of $Z_n^{\pm 1}$ is non-zero on the optical axis due to the existence of J_0 in the integral and the focal fields on the optical axis is circularly polarized. For azimuthally polarized pupil field $Z_n^{\pm 1}$, two focal spots along the optical axis appear symmetrically to the focal plane $z_f = 0$ for $n > 1$ and as n increases, the separation between the two foci increases.

2.4. FOCAL FIELD SHAPING

In this chapter, we only use Z_n^m with the same topological charge m for shaping the focus, and this makes the focal intensity circularly symmetric around the optical axis. The focal fields E_f^m on a given grid in the (x_f, z_f) -plane corresponding to each radially or azimuthally polarized Zernike polynomial are pre-calculated using the FFT and stored in the database. The focal field of a general polarized electric pupil field can be written

as as a linear combination of these basic functions:

$$\mathbf{E}_f = \sum_p \beta_n^m \mathbf{E}_f^{nm}, \quad (2.31)$$

where m is fixed and $p = (n - |m|)/2$.

The optimisation algorithm works as follows:

1. From the database that stores the focal fields, we take the values for each topological charge the $\mathbf{E}_f^{m|m|}(x_f, 0)$ along the x_f axis in the $z_f = 0$ plane. The lateral position where $I_t^{m|m|} = |E_{f,x}^{m|m}|^2 + |E_{f,y}^{m|m}|^2$ gets its maximum is different from the lateral position where $I_z^{m|m|} = |E_{f,z}^{m|m}|^2$ gets its maximum. x_{z0} and x_{t0} are determined correspondingly at the maximum of the contribution of the longitudinal component $I_z^{m|m|}$ and contributions of the transverse components $I_t^{m|m|}$;
2. $\mathbf{E}_f^{nm}(z_f)|_{x_f=x_{z0}}$ and $\mathbf{E}_f^{nm}(z_f)|_{x_f=x_{t0}}$, defined over two axial lines $z_f \in [-z_{max}, z_{max}]$ with separate lateral position x_{z0} and x_{t0} are taken from the database as the basic focal fields for optimisation;
3. A target intensity function I_{target} is defined over $z_f \in [-z_{max}, z_{max}]$;
4. A set of Zernike coefficients β_n^m are randomly generated. The total focal intensity generated by the set of Zernike coefficients is $I = |\mathbf{E}_f|^2$, its longitudinal component contribution is $I_z = |E_{f,z}|^2$ and the transverse component contribution is $I_t = |E_{f,x}|^2 + |E_{f,y}|^2$. For the optimisation of the longitudinal polarization, fields on line $x_f = x_{z0}$ is chosen and $I_z(z_f)|_{x_f=x_{z0}}$ is normalised to $\tilde{I}_z(z_f) = I_z(z_f)|_{x_f=x_{z0}} / I_{max}$, where I_{max} is the maximum total intensity in the xz plane. For optimisation of the transverse polarization, fields on line $x_f = x_{t0}$ is chosen and $I_t(z_f)|_{x_f=x_{t0}}$ is normalised to $\tilde{I}_t(z_f) = I_t(z_f)|_{x_f=x_{t0}} / I_{max}$.
5. Matlab built-in function *lsqnonlin* is used with a 'trust-region-reflective' algorithm to minimize $|\tilde{I}_z - I_{target}|$ for longitudinal component optimisation or $|\tilde{I}_t - I_{target}|$ for transverse component optimisation with the randomly generated set of Zernike coefficients in step 4, and it will generate a set of Zernike coefficient as a result of the minimization. After this, $\sum_{z_f} |\tilde{I}_z - I_{target}|^2$ or $\sum_{z_f} |\tilde{I}_t - I_{target}|^2$ is evaluated;
6. Step 4 and 5 are repeated until $\sum_{z_f} |\tilde{I}_z - I_{target}|^2$ or $\sum_{z_f} |\tilde{I}_t - I_{target}|^2$ is below a certain value;
7. The Zernike coefficients obtained in step 6 are considered as a good starting point of the optimisation. Then a Nelder-Mead simplex direct search method is used to optimize the coefficients in order to get a minimum of $|\tilde{I}_z - I_{target}|$ for the longitudinal component optimisation or $|\tilde{I}_t - I_{target}|$ for the transverse component optimisation.

A few examples are given in the following section:

2.4.1. LONGITUDINALLY POLARIZED ELONGATED SUBWAVELENGTH HOLLOW CHANNEL

An elongated subwavelength hollow channel can be used to trap absorbing nano-particles [12] and cold atoms [13]. It can also be used as an excitation beam for high resolution fluorescence microscope like STED [14].

The z-component $E_{f,z}^{nm}$ of the focused field due to a radially polarized Z_n^m pupil field for given fixed $m \neq 0$ vanishes on the optical axis and has the same topological charge as the incident beam. However its transverse components are not zero on the optical axis. In the optimisation process, we therefore try to maximize the z-component by minimizing $|I_z/I_{max} - I_{target}|$, where $I_z = |\sum_p \beta_n^1 E_{f,z}^{n1}|^2$, I_{max} is the maximum intensity in the xz plane, and the target function I_{target} is a rectangle function along z_f axis with value 1 between $|z_f| < z_{max}$, where $2 \times z_{max}$ is the desired depth of focus.

We use a combination of 14 radially polarized Zernike polynomials $\hat{e}_\rho[Z_n^1]_{n=1,3,5,\dots,27}$ on the exit pupil of an optical system with NA=0.99. As shown in Fig. 2.3, with a set of Zernike coefficients $[\beta_n^1]_{n=1,3,5,\dots,27} = [-0.1437, -0.3, -0.398, -0.589, -0.568, -0.824, -0.674, -0.892, -0.785, -0.743, -0.754, -0.73, -0.182, -0.829]$, we get a hollow spot which is dominated by the longitudinal polarization with a lateral resolution (FWHM) of 0.28λ . Its FWHM of depth of focus is about 16λ , with a good uniformity over a range of 12λ around the focal plane or equivalent to 12.24 Rayleigh unit λ/NA^2 for an optical system with a high NA=0.99. The corresponding radially polarized pupil field with $m = 1$ to generate this elongated hollow spot is shown in Fig. 2.4 which is calculated by $\mathbf{E}_s(\rho, \phi) = \sum_n \hat{e}_\rho \beta_n^1 Z_n^1(\rho, \phi)$.

The ratio of the transverse and longitudinal components can be adjusted by engineering of the low spatial frequency and high spatial frequency components of the pupil field. One common method is to use an annular aperture. For instance, a radially polarized annular pupil with a phase vortex $m = 1$: $A(0.99 < \rho < 1) = \hat{e}_\rho \exp(i\phi)$ and 0 elsewhere in the exit pupil can also generate an elongated subwavelength hollow channel, as shown in Fig. 2.5, but the uniformity of the spot along z dimension is much worse than the results obtained with our method.

2.4.2. ON-AXIS CIRCULARLY POLARIZED FOCAL FIELD

Modulating the local polarization of the focal field by engineering the pupil field can be used to determine the orientation of a single optical emitter[15].

In the first example, a longitudinally polarized elongated hollow channel is generated with the radially polarized pupil field composed of an optimized set of Zernike polynomials Z_n^1 . With a set of radially polarized Zernike polynomials Z_n^1 , we can also maximize the transverse components by optimizing the β_n^1 to minimize $|I_t/I_{max} - I_{target}|$, where $I_t = |\sum_p \beta_n^1 E_{f,x}^{n1}|^2 + |\sum_p \beta_n^1 E_{f,y}^{n1}|^2$, I_{max} is the maximum total intensity in the xz plane, the target function I_{target} is a rectangle function along z_f axis with value 1 between $|z_f| < z_{max}$, where $2 \times z_{max}$ is the desired depth of focus.

We use a combination of 14 radially polarized Zernike polynomials $\hat{e}_\rho[Z_n^1]_{n=1,3,5,\dots,27}$ on the exit pupil of an optical system with NA=0.9. As shown in Fig. 2.6, with the set of Zernike coefficients $[\beta_n^1]_{n=1,3,5,\dots,27} = [-0.2632, 0.7, -0.677, -0.09, 0.982, -1.273, 0.413, 0.553, -1.167, 0.208, -0.194, 0.135, -2.244, 0.586]$, we get an circularly polarized elongated

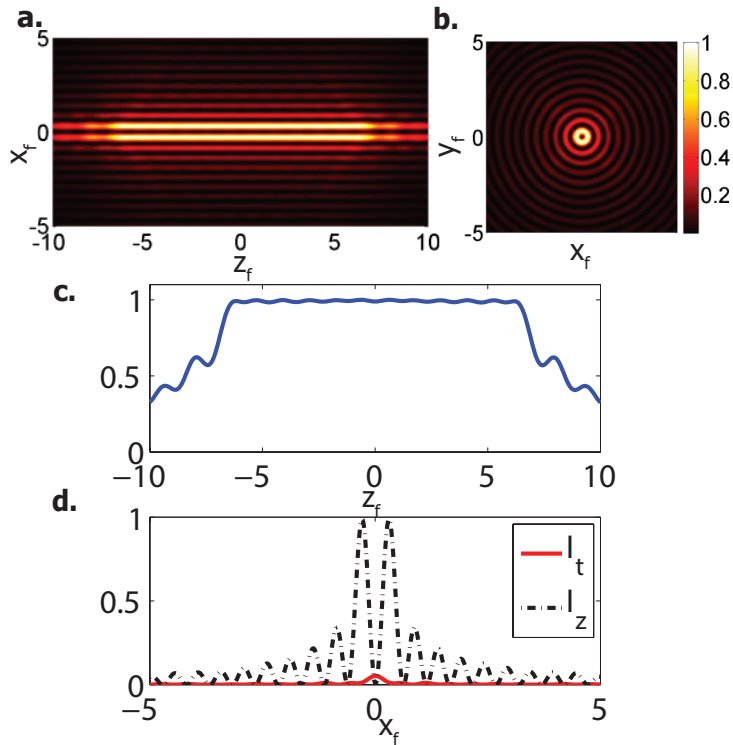


Figure 2.3: The elongated subwavelength hollow spot by the radially polarized phase vortex beam with $m = 1$ obtained by the optimized set of Zernike coefficients in session 2.4.1 on the exit pupil, NA=0.99. (a). Normalised intensity distribution in the $x_f - z_f$ plane (coordinates are in unit of incident light's wavelength); (b). Normalised intensity in $z_f = 0$ plane; (c). The focal intensity distribution along the z_f axis, while its lateral position x_f is located at the maximum of the total intensity in the transversal plane. (d). Focal intensity distribution along x_f axis, its axial position is located at $z_f = 0$.

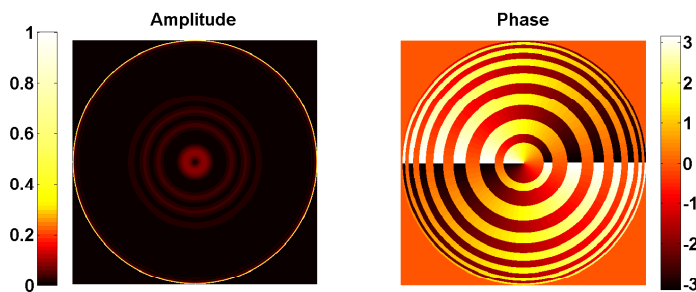


Figure 2.4: The pupil field of the radially polarized phase vortex beam with $m = 1$ to generate the elongated subwavelength hollow spot in Fig. 2.3.

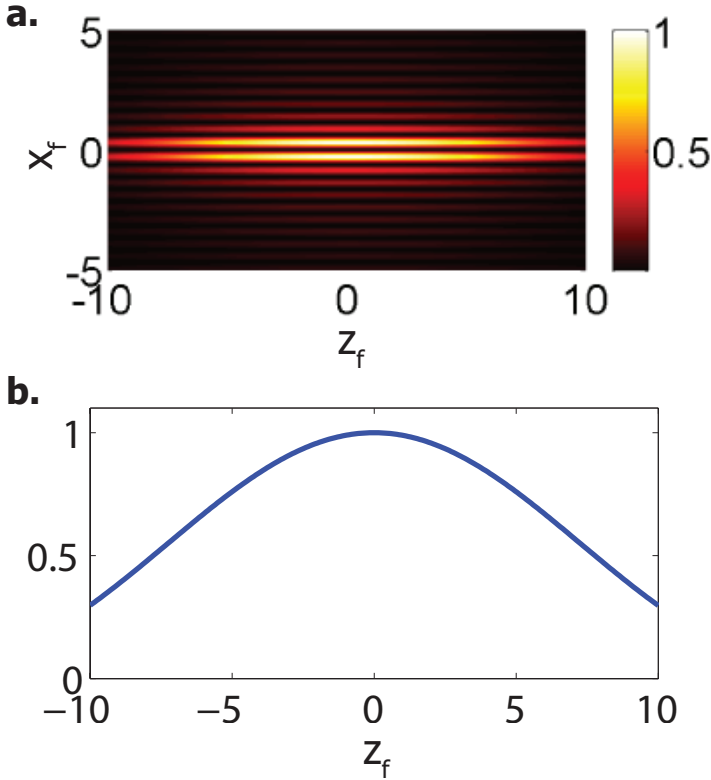


Figure 2.5: The elongated subwavelength hollow spot by a radially polarized annular aperture with phase vortex $m = 1$ on the exit pupil, NA=0.99. (a). Normalized focal intensity distribution in the $x_f - z_f$ plane (coordinates are in unit of incident light's wavelength); (b). Focal intensity distribution along the z_f axis, while its lateral position x_f is located at the maximum of the total intensity in the transversal plane.

focal spot on the optical axis. The longitudinal component contribution to the total intensity is much weaker compared to the transverse component contribution.

The pupil field of the radially polarized phase vortex beam with $m = 1$ to generate this elongated circularly polarized focal spot is then obtained from $\mathbf{E}_s(\rho, \phi) = \hat{e}_\rho \sum_n \beta_n^1 Z_n^1(\rho, \phi)$, as shown in Fig. 2.7.

2.4.3. ON-AXIS MULTIPLE CIRCULARLY POLARIZED FOCAL SPOTS

Multiple subwavelength excitation focal spots along the optical axis can be very useful for fluorescence microscopy, as it can excite the fluorescence simultaneously at multiple planes in the specimen. P.P. Mondal proposed a method using the interference of two counter-propagating long depth of focus PSFs to generate multiple excitation spot PSF [33]. However, this approach utilizes a 4π configuration, which requires more complex optical setup than just shaping the pupil field. From Section 2, we know that for

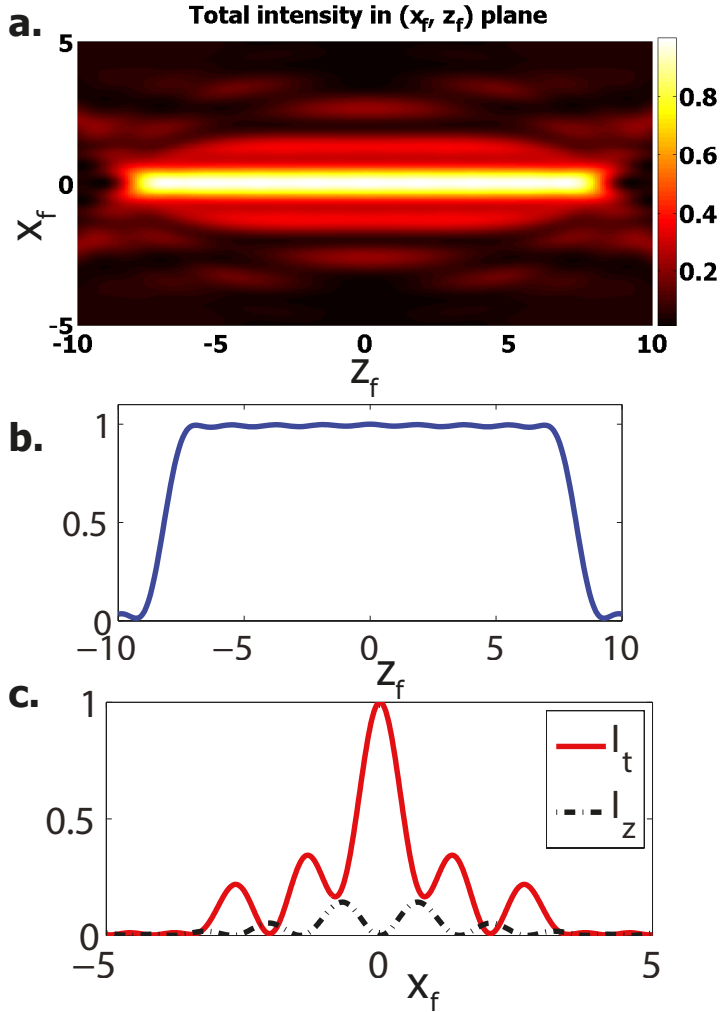


Figure 2.6: The elongated focal spot with stronger transversal polarisation components by the radially polarized phase vortex beam with $m = 1$ obtained by the optimized set of Zernike coefficients in session 2.4.2 on the exit pupil, NA=0.9. (a). The normalised focal intensity distribution in the $x_f - z_f$ plane (coordinates are in unit of incident light's wavelength); (b). Focal intensity distribution along the optical axis; (c). Transversal and longitudinal components of the focal intensity distribution along x_f axis.

Zernike polynomials with a fixed m and $n > |m|$, dual foci appear symmetrically to the focal plane $z_f = 0$, and as n increases, the separation between these two foci increases. By assigning certain Zernike coefficients to the Zernike polynomials Z_n^m with different n , we can generate multiple axial focal spots by shaping the field on the exit pupil.

We use a combination of 14 azimuthally polarized Zernike polynomials $\hat{e}_\phi[Z_n^1]_{n=1,3,5,\dots,27}$ on the exit pupil of an optical system with NA=0.99. As shown in Fig. 2.8, with the set of

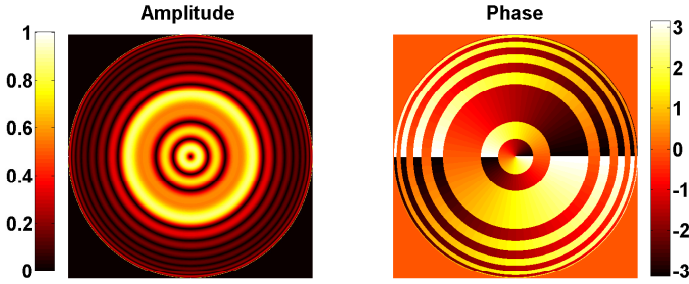


Figure 2.7: The pupil field of the shaped radially polarized phase vortex beam with $m = 1$ to generate the elongated transversally polarized focal spot in Fig. 2.6.

Zernike coefficients $[\beta_n^1]_{n=1,3,5,\dots,27} = [-0.222, 0.228, 0.4726, -0.106, 0.4315, 0.853, -0.169, -0.0438, 0.9424, 0.482, -0.85, 0.824, 0.557, 0.115]$, we get 8 axial focal spots, each with a lateral resolution of 0.216λ and separated about 1.7λ between adjacent spots along the optical axis. The maximum intensity of these focal spots of the azimuthally polarized phase vortex of $m = 1$ lies on the optical axis and contains no longitudinal component. The pupil field of an shaped azimuthally polarized phase vortex with $m = 1$ to generate this multiple focal spots along optical axis is obtained from $\mathbf{E}_s(\rho, \phi) = \sum_n \hat{e}_\phi \beta_n^1 Z_n^1(\rho, \phi)$, as shown in Fig. 2.9.

2.5. DISCUSSIONS

There are also other complete set of orthogonal polynomials used in describing vortex beams and can be used for focal field optimisation, for instance the Laguerre-Gauss (LG) polynomials [34]. Different from Zernike polynomials, the LG polynomials are orthogonal on an infinite plane. For optical imaging systems which often have circular apertures, while using the LG polynomial expansion, one has to take into account the apodization effect, determined by the relative beam size and the actual aperture size. The influence of the apodization has been discussed in Ref. [35]. This will largely increase complexity of the optimisation problem, as more variables need to be considered. In this sense, the Zernike polynomials are simpler and more suitable for finding the desired pupil field of the desired focal field distribution for an optical system with apertures, as it forms a complete set on the unit disk.

There have been great progress in recent years on experimental realization of vector beam. One possible way to generate pupil fields in previous examples is to use Spatial Light Modulators, it has been proven by several works [5–7] that complete control of polarization, amplitude and phase are possible. Vector vortex beams have also been demonstrated by q-plates [36]. With the development of these techniques, the radially /azimuthally polarized pupil field with phase vortices proposed should be realized experimentally.

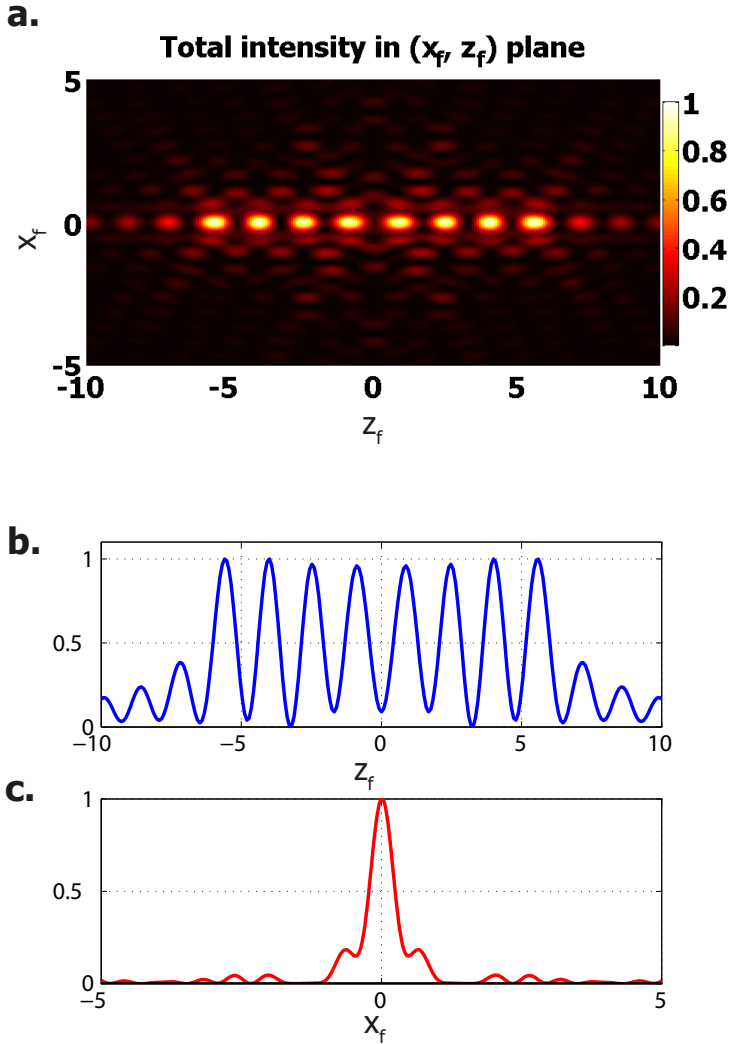


Figure 2.8: Multiple focal spots along the optical axis by the shaped azimuthally polarized phase vortex with $m = 1$ obtained by the optimized set of Zernike coefficients in session 2.4.3 on the exit pupil, $\text{NA}=0.99$. (a). Normalised focal intensity distribution in the (x_f, z_f) plane (coordinates are in unit of incident light's wavelength); (b). Focal intensity distribution along the optical axis; (c). Focal intensity distribution along the x_f axis, z_f is at one of the locations where the spot has maximum intensity on axis.

2.6. CONCLUSION

In this chapter, the focal field of radially or azimuthally polarized complex Zernike polynomials is investigated. Based on the understanding of this, a method to shape the focal field of radially or azimuthally polarized pupil field with a phase vortex is proposed. With pre-calculation of the focal field of each radially and azimuthally polarized Zernike poly-

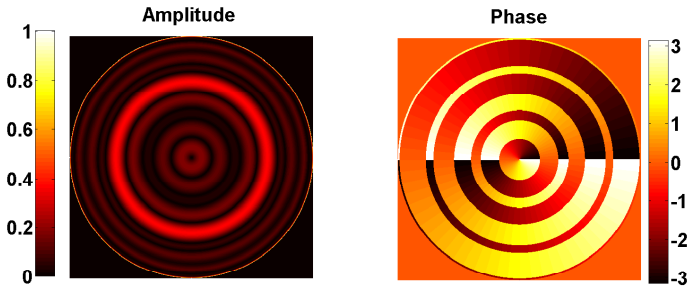


Figure 2.9: The pupil field of the shaped azimuthally polarized phase vortex with $m = 1$ to generate multiple focal spot along optical axis in Fig. 2.8.

nomial, the optimization variables are reduced to the number of Zernike coefficients being used. Three results based on this method are given in this chapter, including a longitudinally polarized subwavelength hollow channel with a depth of focus up to 12λ and a lateral resolution (FWHM) of 0.28λ for an optical system with $\text{NA}=0.99$. By engineering the ratio of high and low spatial frequencies of the pupil field, a transversally polarization dominated elongated focal spot is obtained with a set of radially polarized Zernike polynomials with a topological charge of 1. We also obtained multiple subwavelength focal spots along the optical axis. With these results, the pupil shaping of azimuthally and radially polarized optical vortices can achieve resolution improvement of optical systems and can shape the polarization and intensity distribution in the focal region, which may result in interesting applications in the area of high resolution fluorescence microscopy, optical trapping, etc.

REFERENCES

- [1] L. Wei and H.P. Urbach, *Shaping the focal field of radially/azimuthally polarized phase vortex with zernike polynomials*, Journal of Optics **18**, 065608 (2016).
- [2] K. Youngworth and T.G. Brown, *Focusing of high numerical aperture cylindrical vector beams*, Opt. Express **10**, 77 (2000).
- [3] Q.W. Zhan and J.R. Leger, *Focus shaping using cylindrical vector beams*, Opt. Express **10**, 324 (2002).
- [4] Q.W. Zhan, *Cylindrical vector beams: from mathematical concepts to applications*, Advances in Optics and Photonics **1**, 1 (2009).
- [5] W. Han, Y.F. Yang, W. Cheng and Q.W. Zhan, *Vectorial optical field generator for the creation of arbitrarily complex fields*, Opt. Express **21**, 20692 (2013).
- [6] Z.Z. Chen, T.T. Zeng, B.J. Qian and J.P. Ding, *Complete shaping of optical vector beams*, Opt. Express **23**, 17701 (2015).
- [7] Z.Y. Rong, Y.J. Han, S.Z. Wang and C.S. Guo, *Generation of arbitrary vector beams with cascaded liquid crystal spatial light modulators*, Opt. Express **22**, 1636 (2014).
- [8] V. D'Ambrosio, F. Baccari, et al., *Arbitrary, direct and deterministic manipulation of vector beams via electrically-tuned q-plates*, Scientific Reports **5**, 7840 (2015).
- [9] Z. Liu, Y. Liu, et al., *Generation of arbitrary vector vortex beams on hybrid-order poincaré sphere*, Photonics Research **5**, 15 (2017).
- [10] D. Naidoo, E.S. Roux et al., *Controlled generation of higher-order poincaré sphere beams from a laser*, Nature Photonics **10**, 327 (2016).
- [11] K. Lalithambigai, P. Suresh, V. Ravi, K. Prabakaran, Z. Jaroszewicz, K.B. Rajesh, P.M. Anbarasan and T.V.S. Pillai, *Generation of sub wavelength super-long dark channel using high na lens axicon*, Opt. Lett. **37**, 999 (2012).
- [12] C. Alpmann, M. Esseling, P. Rose and C. Denz, *Holographic optical bottle beam*, App. Phy. Lett. **100**, 111101 (2012).
- [13] P. Xu, X.D. He, J. Wang and M.S. Zhan, *Trapping a single atom in a blue detuned optical bottle beam trap*, Opt. Lett. **35**, 2164 (2010).
- [14] K.I. Willig, S.O. Rizzoli, V. Westphal, R. Jahn and S.W. Hell, *Sted microscopy reveals that synaptotagmin remains clustered after synaptic vesicle exocytosis*, Nature **440**, 935 (2006).
- [15] N. Huse, A. Schonle and S.W. Hell, *Z-polarized confocal microscopy*, J. Biomed. Opt. **6**, 480 (2001).
- [16] M. Kasperczyk, S. Person, D. Ananias, L.D. Carlos and L. Novotny, *Excitation of magnetic dipole transitions at optical frequencies*, Phys. Rev. Lett. **114**, 163903 (2015).

- [17] L.E. Helseth, *Optical vortices in focal regions*, Opt. Commun. **229**, 85 (2004).
- [18] C.J.R. Sheppard, *Polarized focused vortex beams: half-order phase vortices*, Opt. Express **22**, 18128 (2014).
- [19] X. Hao, C.F. Kuang, T.T. Wang and X. Liu, *Phase encoding for sharper focus of the azimuthally polarized beam*, Opt. Lett. **35**, 3928 (2010).
- [20] Y. Kozawa and S. Sato, *Dark-spot formation by vector beams*, Opt. Letters **33**, 2326 (2008).
- [21] Y.Q. Zhao, J.S. Edgar, G.D.M. Jeffries, D. McGloin and D.T. Chiu, *Spin-to-orbital angular momentum conversion in a strongly focused optical beam*, Phys. Rev. Letters **99**, 073901 (2007).
- [22] H.F. Wang, L.P. Shi, B. Lukyanchuk, C. Sheppard and C.T. Chong, *Creation of a needle of longitudinally polarized light in vacuum using binary optics*, Nature photonics **2**, 501 (2008).
- [23] J.M. Wang, W.B. Chen and Q.W. Zhan, *Engineering of high purity ultra-long optical needle field through reversing the electric dipole array radiation*, Opt. Express **18**, 21965 (2010).
- [24] J.M. Wang, Q.L. Liu, C.J. He and Y.W. Liu, *Reversal construction of polarization-controlled focusing field with multiple focal spots*, Optical Engineering **52**, 048002 (2013).
- [25] Y.Z. Yu and Q.W. Zhan, *Creation of identical multiple focal spots with prescribed axial distribution*, Sci. Reports **5**, 14673 (2015).
- [26] B. Richards and E. Wolf, *Electromagnetic diffraction in optical systems ii. structure of the image field in an aplanatic system*, Proc. R. Soc. Lond. A **253**, 358 (1959).
- [27] L. Novotny and B. Hecht, *Principles of nano-optics* (Cambridge university press, 2012).
- [28] H. P. Urbach, *Lecture notes on theoretical optics* (2017).
- [29] M. Leonard and E. Wolf, *Optical coherence and quantum optics* (Cambridge university press, 1995).
- [30] J.J.M. Braat, S. van Haver, A.J.E.M. Janssen and P. Dirksen, *Assessment of optical systems by means of point-spread functions*, Progress in Optics **51**, 349 (2008).
- [31] S. van Haver and A.J.E.M. Janssen, *Advanced analytical treatment and efficient computation of the diffraction integrals in the extended nijmegen zernike theory*, J. Europ. Opt. Soc. Rap. Public. **8**, 13044 (2013).
- [32] M. Leutenegger, R. Rao, R.A. Leitgeb and T. Lasser, *Fast focus field calculations*, Opt. Express **14**, 11277 (2006).

- [33] S. Dilipkumar and P.P. Mondal, *High resolution multiple excitation spot optical microscopy*, AIP Advances **1**, 02128 (2011).
- [34] L. Allen and M.J. Padgett, *The poynting vector in laguerre-gaussian beams and the interpretation of their angular momentum density*, Opt. Comm. **184**, 67 (2000).
- [35] P.L. Overfelt and C.S. Kenney, *Comparison of the propagation characteristics of bessel, bessel-gauss and gaussian beams diffracted by circular aperture*, J. Opt. Soc. Am. A. **16**, 1286 (1999).
- [36] F. Cardano, E. Karimi, S. Slussarenko, L. Marrucci, C. de Lisio and E. Santamato, *Polarization pattern of vector vortex beams generated by q-plate with different topological charges*, Applied Optics **51**, C1 (2012).

3

EXCITATION OF THE RADIATIONLESS ANAPOLE MODE

The existence of non-radiating sources is of fundamental importance for inverse scattering problems and design of invisible objects. However, excitation of such radiationless sources is quite challenging. We present a method based on which the anapole mode of a high index isotropic dielectric nanosphere can be excited but radiationless. We show that this radiationless anapole is attributed to the destructive interference of the Cartesian dipole and toroidal moment of the induced current by our proposed focused radially polarized beam illumination. Further, with a standing wave illumination formed by two counter-propagating focused radially polarized beam under 4π configuration, the ideal radiationless anapole can be excited. This result illustrates a case where the reciprocity condition is not violated and yet a radiationless mode can be excited by external illumination.

3.1. INTRODUCTION

Objects that cannot be seen have been a fascinating possibility both in popular imagination and in the scientific community. Besides the practical implications in modern day security applications it is also of great interest in the general scientific study of the universe [2]. There are different possible types of these objects which are radiationless. These can be objects which do not scatter incident light [3]. There also can be time varying charge or current distributions or atoms which do not radiate [4–7]. The study of such non-radiative objects has been a part of fundamental physics for a long time [8–10]. Studies have aimed to understand the physics of these objects from scattering from non-absorbing particles [3], inverse scattering problems [6, 11] and metamaterials to suppress radiation loss [12, 13] to mention a few. Possible applications of this physics for designing non-scattering objects are also being investigated [14].

One such case of non-radiating sources is the anapole. This was first introduced in elementary particle physics [15] and recently has been of interest in particle physics again [2]. The anapole mode arises when the electrical dipole and toroidal dipole moment form a nontrivial destructive interference [16–18]. However, it is until recently that the nonradiating anapole mode is experimentally demonstrated [19, 20]. In Mie scattering theory, under certain conditions, a specific multipole mode from the multipole decomposition of the scattering field of an illuminated particle, can be completely suppressed. For example, the scattering coefficient of the spherical electric dipole moment can be zero at certain wavelength for a high index dielectric nanosphere under plane wave illumination [21]. However, at the same time a strong and broadband magnetic dipole resonance can be excited in the high index dielectric nanosphere [22, 23]. Therefore the nonradiating anapole mode of a nanosphere is difficult to observe under plane wave illumination due to simultaneous excitation of electric and magnetic modes. That's why the first experimental demonstration of anapole in the visible wavelength range [20] is done with a specially designed nanodisk, instead of a sphere. In spite of constructing the nanodisk for the specific anapole condition, the scattering from the particle cannot be completely reduced to zero due to the simultaneous excitation of a magnetic quadrupole mode. Instead of specifically designed structures [20, 24], in this work we propose an alternative way to excite the anapole mode of an isotropic nanosphere with tightly focused radially polarized beams. The focused radially polarized beam, which has a pure longitudinally polarized electric field E_z and zero magnetic field at the focal point [25] can keep all the magnetic modes suppressed and efficiently induced a current that does not radiate electric dipole mode at the anapole condition except for a weak electric quadrupole. In addition we show that when two focused radially polarized beams under 4π configuration illuminate the nanosphere, the electric quadrupole radiation is completely suppressed and an ideal radiationless anapole is excited.

3.2. SINGLE BEAM EXCITATION

The configuration of the proposed anapole excitation is shown in Fig. 3.1(a), where a tightly focused radially polarized beam illuminates a high index dielectric nanosphere of radius $r_0 = 100$ nm and refractive index $n = 3.5$, placed at the focal point. The sur-

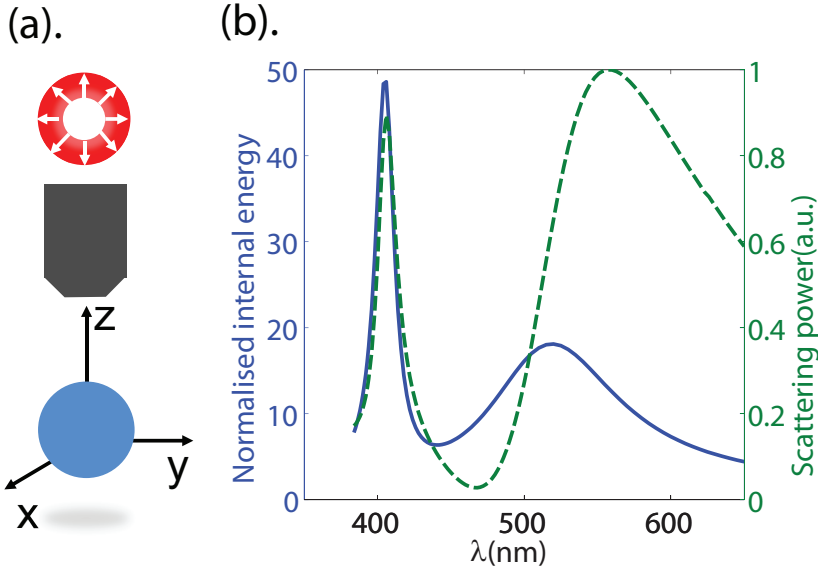


Figure 3.1: (a). A dielectric nanosphere of refractive index $n=3.5$ and radius $r_0 = 100$ nm is illuminated by a focused radially polarized beam in an optical system with numerical aperture $NA=0.86$; (b). Normalized energy inside the particle and the scattering power for a dielectric nanosphere at the focus of a radially polarized beam.

rounding medium is air but the result holds for any high index sphere embedded in a low index, homogeneous and isotropic medium. In the numerical implementation, the focal field of the radially polarized beam is calculated by the Richard-Wolf diffraction integral [26] and then imported to a finite element method simulation [27] to calculate the scattering properties of the nanosphere. In Fig. 3.1(b) we show the calculated spectral dependence of the scattering power and the internal energy of the particle. Here the electrical energy inside the particle $W_E = \frac{1}{2} \int_{sph} \mathbf{E} \cdot \mathbf{E}^* d^3\mathbf{r}$ is normalized to the focal energy $W_f = \frac{1}{2} \int_{sph} \mathbf{E}_f \cdot \mathbf{E}_f^* d^3\mathbf{r}$ within the same volume of the sphere $sph = \{\mathbf{r} : |\mathbf{r}| \leq r_0\}$, when the particle is absent. We can clearly see from the scattering power spectrum in Fig. 3.1(b) that only electric modes are excited while the magnetic modes, including the magnetic quadruple resonance at $\lambda = 505$ nm, are suppressed. This selective excitation of electric modes by focused radially polarized beam has been shown in previous works [28–30] and can be explained explicitly by multipole expansion of the focal field [31]:

$$\mathbf{E}_f(\mathbf{r}) = \sum_{l=1}^{\infty} [p_{El}^0 \mathbf{N}_l^0(\mathbf{r}) + p_{Ml}^0 \mathbf{M}_l^0(\mathbf{r})] \quad (3.1)$$

where p_{El}^0 and p_{Ml}^0 are the strengths of the electric and magnetic components which can be analytically calculated by Eq. (10) in Ref. [31]. As is shown in Ref. [31], $p_{Ml}^0 = 0$, i.e. all the magnetic multipole components are zero for focused radially polarized beam. We also observe from Fig. 3.1(b), that at $\lambda = 464$ nm, the scattering power is at the minimum but the internal energy of the particle is 8 times higher than the energy at the

focal volume of the illumination, when no particle is present. This is a clear indication that an induced current distribution exists inside the particle, while very little radiation is present outside.

In order to decide that whether an anapole moment is excited, the field inside the particle is numerically calculated and Cartesian multipole moment analysis [20] is applied on the induced current

$$\mathbf{J} = -i\omega(n^2 - 1)\mathbf{E} \quad (3.2)$$

inside the particle. The focused radially polarized beam induces an inhomogenous current distribution inside the particle. It excites not only the Cartesian dipole moment

$$\mathbf{P} = \frac{i}{\omega} \int_{sph} \mathbf{J} d^3\mathbf{r}, \quad (3.3)$$

but also the toroidal dipole moment

$$\mathbf{T} = \frac{1}{10c} \int_{sph} [(\mathbf{r} \cdot \mathbf{J})\mathbf{r} - 2r^2\mathbf{J}] d^3\mathbf{r}. \quad (3.4)$$

The toroidal dipole moment, featuring an electric poloidal current with a circulating magnetic field, has exactly the same far field scattering pattern as a Cartesian dipole moment. An anapole is excited if the condition $\mathbf{P} = -ik\mathbf{T}$ is fulfilled, where the electrical dipole moment and toroidal moment interfere destructively with each other, resulting in complete cancellation of their far field radiation. The z component of the Cartesian dipole moment \mathbf{P} and toroidal moment $ik\mathbf{T}$ of the high index nanosphere in Fig. 3.1(a) are calculated numerically and illustrated in Fig. 3.2. Due to cylindrical symmetry around the optical axis of both the focal field of radially polarized beam and the nanosphere, the induced current \mathbf{J} is also cylindrically symmetric, which can be seen from the inserted figure about the electric field distribution inside the particle in Fig. 3.2(a). As a result of this symmetry, both the electric dipole moment \mathbf{P} and the toroidal moment \mathbf{T} have only the z component as a non zero component. The minima in the scattering power seen in Fig. 3.1 at $\lambda = 464$ nm is explained by the wavelength dependent plots of the electric dipole moment \mathbf{P} and the toroidal moment \mathbf{T} seen in Fig. 3.2. Here we observe that at this wavelength the anapole mode condition $P_z = -ikT_z$ is fulfilled such that the scattering fields of dipole and toroidal moment have the same strength but are out of phase, resulting in complete cancellation of the far field dipole mode radiation.

From Fig. 3.1(b), we can see that even at the anapole condition $\lambda = 464$ nm, the scattering is not completely suppressed. This is confirmed by the radiation pattern in Fig. 3.3. Here we clearly see that though the peak scattering power at $\lambda = 464$ nm is 40 times weaker compared to the electric dipole resonance at $\lambda = 554$ nm, it is not zero. Since both electric dipole and toroidal moment have only z component, the strength of the far field dipole radiation can be evaluated in the $z = 0$ plane. As shown in Fig. 3.3(a), the scattering power in $z = 0$ plane is zero at $\lambda = 464$ nm. Therefore though the farfield dipole radiation of the induced current in the nanosphere is cancelled by the destructive interference of the Cartesian dipole moment and toroidal moment, a weak electric quadrupole mode is excited at the same wavelength and results in nonzero total scattering.

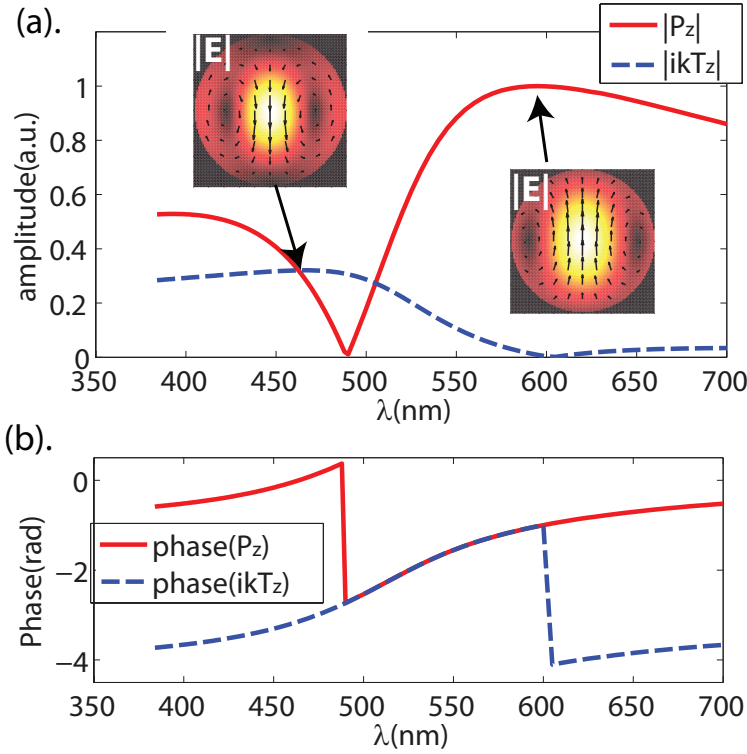


Figure 3.2: (a) Amplitude and (b) phase of Cartesian dipole moment P_z and toroidal moment ikT_z of the induced current inside the particle at focus. The left inserted figure in (a) shows the induced current distribution at wavelength $\lambda = 464$ nm where the anapole mode is excited, the right inserted figure in (a) shows the pure dipole mode.

3.3. "IDEAL" RADIATIONLESS ANAPOLE EXCITATION UNDER 4π CONFIGURATION

In a second example we show that an ideal radiationless anapole can be realized with an excitation field formed by the interference of two counterpropagating focused radially polarized beams under a 4π configuration, as illustrated in Fig. 3.4. The two beams have exactly the same amplitude distribution but a π phase difference. Based on Eq.(10) in Ref. [31], we can get the strength of electric multipoles for the 4π excitation field:

$$p_{El}^0 = -\frac{i^l \sqrt{\pi(2l+1)}}{l(l+1)} \left\{ \int_0^{\theta_m} A(\alpha) \frac{\partial P_l(\cos \alpha)}{\partial \alpha} \sin \alpha d\alpha - \int_{\pi}^{\pi-\theta_m} A(\pi-\alpha) \frac{\partial P_l(\cos \alpha)}{\partial \alpha} \sin \alpha d\alpha \right\}, \quad (3.5)$$

where $A(\alpha)$ is the amplitude distribution of the radially polarized beam and $\sin \theta_m$ is the numerical aperture. By putting the corresponding Legendre function $P_2(\cos \alpha)$ into Eq. (3.5), we can get that $p_{E2}^0 = 0$, i.e. the 4π excitation field doesn't contain electric quadrupole.

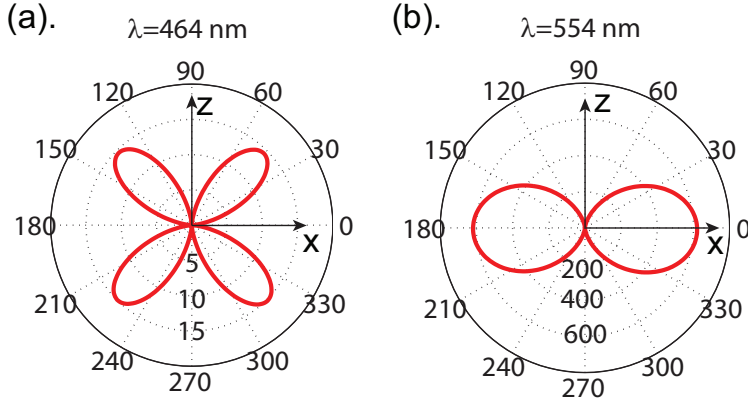


Figure 3.3: Radiation pattern (radiation power in arbitrary units) of the particle illuminated by a focused radially polarized beam in xz plane at the wavelengths of (a) anapole mode and (b) electric dipole mode.

ple component so that the electric quadruple mode of the scattering nanosphere cannot be excited. The excitation field consists, apart from the nonzero electric dipole component p_{E1}^0 , also a nonzero electric octupole p_{E3}^0 and $|p_{E3}^0| < |p_{E1}^0|$. From Generalized Lorenz-Mie theory (GLMT) [32], the strength of a scattering multipole depends both on the excitation beam and the Mie scattering coefficient [21] a_l of the sphere $E_l \propto |p_{E1} a_l|$. As shown in Fig. 3.4(b), the electric octupole of the high index sphere forms a narrowband resonance at a much shorter wavelength and its Mie coefficient in the wavelength range of our interest ($\lambda > 390$ nm) is below 10^{-2} , making its contribution to the total scattering power negligible. From Fig. 3.4(b), we can see that our FEM calculation of the scattering spectrum matches perfectly with the pure electric dipole scattering spectrum calculated by the analytical GLMT. At the anapole condition $\lambda = 464$ nm, the scattering power of the particle under 4π illumination is nearly zero with the focal field outside the particle unperturbed as shown in Fig. 3.4(d). However, the internal energy is still 8 times higher than the illumination energy in the same spherical volume, implying that an induced current is excited but rarely radiates, *i.e.* an ideal radiationless anapole mode is excited. In Fig. 3.4(e), the scattering field is little outside the particle even in the nearfield. This also complies with a general property of nonradiating sources that the radiation field vanishes everywhere outside the source region [7, 12].

In recent literature it has been speculated whether it is possible to achieve total zero scattering using external sources [20] due to possible violation of the reciprocity theorem. So to examine our proposal for the ideal radiationless anapole under 4π -illumination we consider the following. Let the focal field of the 4π configuration in the absence of the particle, $\mathbf{E}_f^{4\pi}$, be generated by a current $\mathbf{J}_f^{4\pi}$ in the source volume V . Additionally let \mathbf{E}_s be the electric field radiated by the induced current $\mathbf{J} = -i\omega(n^2 - 1)\mathbf{E}$ in the nanosphere. According to the reciprocity theorem [33], we should have

$$\int_{sph} \mathbf{E}_f^{4\pi} \cdot \mathbf{J} d^3\mathbf{r} = \int_V \mathbf{J}_f^{4\pi} \cdot \mathbf{E}_s d^3\mathbf{r}. \quad (3.6)$$

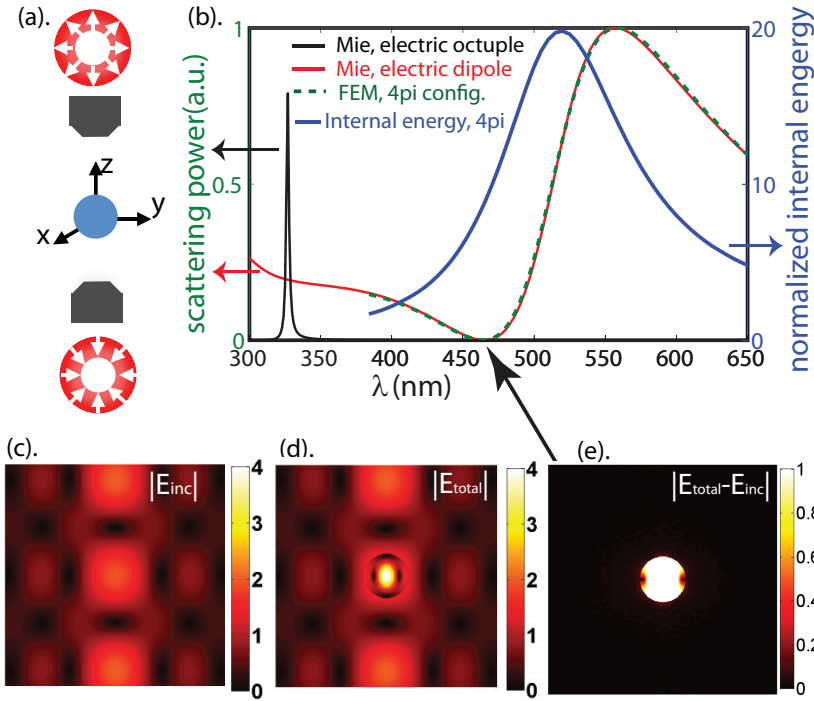


Figure 3.4: (a). 4π illumination configuration, where the two counter-propagating radially polarized beam have exactly the same intensity but π phase difference; (b). The normalized internal energy, the scattering power spectrum of the particle excited under the 4π configuration calculated by FEM and the scattering power spectrum of a pure electric dipole and octupole by Lorenz Mie theory; (c). The focal electrical field of the 4π configuration; (d). Total electric field of the particle excited by the focal field in (c) at the radiating anapole condition $\lambda = 464$ nm; (e) total field subtracted by the illumination field.

For the ideal nonradiating current source \mathbf{J} , the scattering far field \mathbf{E}_s in source volume V should be zero so that implies $\int_V \mathbf{J}_f^{4\pi} \cdot \mathbf{E}_s d^3\mathbf{r} = 0$. For complying with the reciprocity theorem, it only requires that the integral $\int_{sph} \mathbf{E}_f^{4\pi} \cdot \mathbf{J} d^3\mathbf{r}$ to be zero instead of having zero induced current everywhere inside the source volume. It has been numerically verified that this condition is fulfilled by the radiationless anapole mode of the nanosphere excited by the 4π illumination with the extremely weak electric octupole component neglected.

3.4. CONCLUSION

In summary, we demonstrate that it is possible to excite the anapole mode of an isotropic high index dielectric nanosphere by illumination with tightly focused radially polarized beams. With single focused beam excitation, the anapole dipole mode can be excited but there is still a weak contribution of electric quadruple radiation in the total scattering power. However, an ideal radiationless anapole can be excited by a 4π configuration, where the two counter-propagating radially polarized beams have the same amplitude

but a π phase difference, illustrating a condition where the reciprocity condition is not violated and yet a non-radiating mode can be excited by external illumination. This is the first time in our knowledge that a configuration has been found where the non-radiating anapole mode can be excited inside an un-engineered isotropic spherical Mie particle. The anapole moment has to be studied further to understand the physics of the non-scattering objects, nonradiating sources and as an electromagnetic form factor of particles. Applications of this mode in non-invasive sensing, suppression of spurious scattering, design of invisible objects and optical switches where the scattering can be switched on and off with the anapole mode can be possible in the future.

REFERENCES

- [1] L. Wei, Z. Xi, N. Bhattacharya and H.P. Urbach, *Excitation of the radiationless anapole mode*, *Optica* **3**, 799 (2016).
- [2] C.M. Ho and R.J. Scherrer, *Anapole dark matter*, *Phys. Lett. B* **722**, 341 (2013).
- [3] M. Kerker, *Invisible bodies*, *J. Opt. Soc. AmB* **65**, 376 (1975).
- [4] A.J. Devaney and E. Wolf, *Radiating and nonradiating classical current distributions and the fields they generate*, *Phys. Rev. D* **8**, 1044 (1973).
- [5] K. Kim and E. Wolf, *Non-radiating monochromatic sources and their fields*, *Opt. Commun.* **59**, 1 (1986).
- [6] E. Wolf and T. Habashy, *Invisible bodies and uniqueness of the inverse scattering problem*, *J. Mod. Opt.* **40**, 785 (1993).
- [7] G. Gbur, *Nonradiating sources and the inverse source problem*, Ph.D. thesis, University of Rochester, Rochester (2001).
- [8] P. Ehrenfest, *Ungleichförmige elektrizitätsbewegungen ohne magnet- und strahlungsfeld*, *Phys. Z* **11**, 708 (1910).
- [9] G.A. Schott, *The electromagnetic field of a moving uniformly and rigidly electrified sphere and its radiationless orbits*, *Philos. Mag.* **7**, 752 (1933).
- [10] G.H. Goedecke, *Classically radiationless motions and possible implications for quantum theory*, *Phys. Rev.* **135**, B281 (1964).
- [11] B.J. Hoenders, *Existence of invisible nonscattering objects and nonradiating sources*, *J. Opt. Soc. AmA* **14**, 262 (1997).
- [12] M.G. Silveirinha, *Trapping light in open plasmonic nanostructures*, *Phys. Rev. A* **89**, 23813 (2014).
- [13] S. Lannebere and M.G. Silveirinha, *Trapping light in open plasmonic nanostructures*, *Nature Comm.* **6**, 9766 (2015).
- [14] U. Leonhardt, *Optical conformal mapping*, *Science* **312**, 1777 (1993).
- [15] Ya.B. Zel'dovich, *Electromagnetic interaction with parity violation*, *Zh. Eksp. Teor. Fiz* **33**, 1531 (1957).
- [16] V.M. Dubovik and V.V. Tugushev, *Toroidal moments in electrodynamics and solid-state physics*, *Phys. Rep.* **4**, 145 (1990).
- [17] G.N. Afanasiev and Yu.p. Stepanovsky, *The electromagnetic field of elementary time-dependent toroidal sources*, *J. Phy. A: Math. Gen.* **8**, 4565 (1995).
- [18] T. Kaelberer, V.A. Fedotov, N. Papasimakis, D.P. Tsai and N.I. Zheludev, *Toroidal dipolar response in metamaterials*, *Science* **330**, 1510 (2010).

- [19] V.A. Fedotov, V. Rogacheva, V. Savinov, D.P. Tsai and N.I. Zhueludev, *Resonant transparency and non-trivial non-radiating excitations in toroidal metamaterials*, Scientific Rep. **3**, 2967 (2013).
- [20] A.E. Miroschnichenko, A.B. Evlyukhin, Y.F. Yu, R. M. Bakker, A. Chipouline, A.I. Kuznetsov, B. Luk'yanchuk, B.N. Chichkov and Y.S. Kivshar, *Nonradiating anapole modes in dielectric nanoparticles*, Nat. Comm. **6**, 8069 (2015).
- [21] C.F. Bohren and D.R. Huffman, *Absorption and scattering of light by small particles* (Wiley-vch verlag, 1998).
- [22] A.I. Kuznetsov, A.E. Miroschnichenko, Y.H. Fu, J.B. Zhang and B. Luk'yanchuk, *Magnetic light*, Sci. Rep. **2**, 492 (2012).
- [23] A.B. Evlyukhin, S.M. Novikov, U. Zywietz, R.L. Eriksen, C. Reinhardt, S.I. Bozhevolnyi, and B.N. Chichkov, *Demonstration of magnetic dipole resonances of dielectric nanospheres in the visible region*, Nano Lett. **12**, 3479 (2012).
- [24] W. Liu, B. Lei, J.H. Shi, H.J. Hu and A.E. Miroschnichenko, *Elusive pure anapole excitation in homogenous spherical nanoparticles with radial anisotropy*, J. Nanomaterials **2015**, 672957 (2015).
- [25] L. Novotny and B. Hecht, *Principles of nano-optics* (Cambridge university press, 2012).
- [26] B. Richards and E. Wolf, *Electromagnetic diffraction in optical systems ii. structure of the image field in an aplanatic system*, Proc. R. Soc. Lond. A **253**, 358 (1959).
- [27] X.H. Wei, A.J.H. Wachtters and H.P. Urbach, *Finite-element model for three-dimensional optical scattering problems*, J. Opt. Soc. Am.A **24**, 866 (2007).
- [28] P.I. Wozniak, P. Banzer and G. Leuchs, *Selective switching of individual multipole resonances in single dielectric nanoparticles*, Laser and Photonics Rev. **12**, 231 (2012).
- [29] T. Das, P.P. Iyer, R.A. DeCrescent and J.A. Schuller, *Beam engineering for selective and enhanced coupling to multipolar resonances*, Phys. Rev. B **92**, 241110 (2015).
- [30] Z. Xi, L. Wei, A. J. L. Adam, and H. P. Urbach, *Broadband active tuning of unidirectional scattering from nanoantenna using combined radially and azimuthally polarized beams*, Opt. Lett. **41**, 33 (2016).
- [31] T.X. Hoang, X. Chen and C.J.R. Sheppard, *Multipole theory for tight focusing of polarized light, including radially polarized and other special cases*, J. Opt. Soc. Am. A **29**, 32 (2012).
- [32] T.X. Hoang, X. Chen and C.J.R. Sheppard, *Interpretation of the scattering mechanism for particles in a focused beam*, Phys. Rev. A **86**, 33817 (2012).
- [33] L.D. Landau and E.M. Lifshitz, *Electrodynamics of Continuous Media* (Pergamon, Oxford, 1960).

4

ADDING A SPIN TO KERKER'S CONDITION: ANGULAR TUNING OF DIRECTIONAL SCATTERING WITH DESIGNED EXCITATION

We describe a method to control the directional scattering of a high index dielectric nanosphere, which utilizes the unique focusing properties of an azimuthally polarized phase vortex and a radially polarized beam to independently excite inside the nanosphere a spinning magnetic dipole and a linearly polarized electric dipole mode normal to the magnetic dipole. We show that by simply adjusting the phase and amplitude of the field on the exit pupil of the optical system, the scattering of the nanosphere can be tuned to any direction within a plane and the method works over a broad wavelength range.

Parts of this chapter have been published in Optics Letters **42**, 1776 (2017) [1].

4.1. INTRODUCTION

Precise control of the scattering of subwavelength nanostructures is becoming an important research topic with applications for directional coupling of light [2, 3], displacement metrology [4, 5], optical forces [6] and directional excitation of quantum emitters [7], etc.. One way to achieve directional scattering is using high index dielectric nanoparticles which exhibit not only electric modes but also magnetic modes [8, 9]. This unique property makes them low-loss and functional building blocks for nano-antennas, compared to metallic nanostructures. The interference of the magnetic and electric dipole modes of a dielectric nanoparticle under plane wave illumination can lead to zero backward scattering [10], similar to what is theoretically predicted by Kerker et al. [11, 12]. However, for a given particle, the unidirectional scattering can only be realized along the propagation direction of the beam at a single wavelength due to the relation between electric and magnetic field of a plane wave and the properties of Mie coefficients. Independent control of linearly polarized magnetic and electric dipoles has been realized with an excitation configuration composed of orthogonally oriented focused azimuthally and radially polarized beams [13], where directional scattering over a broad wavelength range can be achieved. However, this method needs two focusing optical systems and directional scattering can only be realized along the direction normal to the plane of the electric and magnetic dipoles. A different concept, namely spin-controlled directional coupling of light has drawn lots of attentions and is considered as an example of the spin-orbit interaction of light [14]. Several experiments have demonstrated the spin controlled directional excitation of surface plasmon and waveguide modes, utilizing the near-field interference of a rotating dipole [2, 3], the transverse spin of the evanescent waves [15, 16] and metasurfaces [17]. However, the directional propagation of light controlled by spin is binary, either to one direction or the opposite corresponding to either left or right circularly polarized light. Angular tuning is a desirable function to gain full control over the scattering of light, but rotation of the directional scattering with aforementioned methods often needs to rotate the excitation beams, which is very inconvenient in practice. In the current chapter, a method is proposed to overcome this limitation and tune the scattering of a dielectric nanosphere to any direction within a plane without moving the excitation beam. The approach relies on the independent excitation of a spinning magnetic dipole and a linearly polarized electric dipole mode. Utilizing the unique focusing properties of vector vortex beams, we are able to realize such excitation and achieve arbitrary scattering direction tuning in a plane over a relatively broad wavelength range by simply adjusting the amplitude and phase of the beams.

4.2. BASIC PHYSICAL MODEL

Unlike previous approaches [5, 10, 13] based on the interference of linearly polarized magnetic and electric dipoles, we propose a method to actively control the scattering to any direction in the $z = 0$ plane using the interference of a spinning (circularly polarized) magnetic dipole $\mathbf{m} = m_0(\hat{x} + i\hat{y})$ and an electric dipole $\mathbf{p} = p_0\hat{z}$ linearly polarized in the z direction as illustrated in Fig. 4.1. It is easy to show [18] that the farfield electrical field in the $z = 0$ plane of the electrical dipole is polarized along the z direction and cylindrically

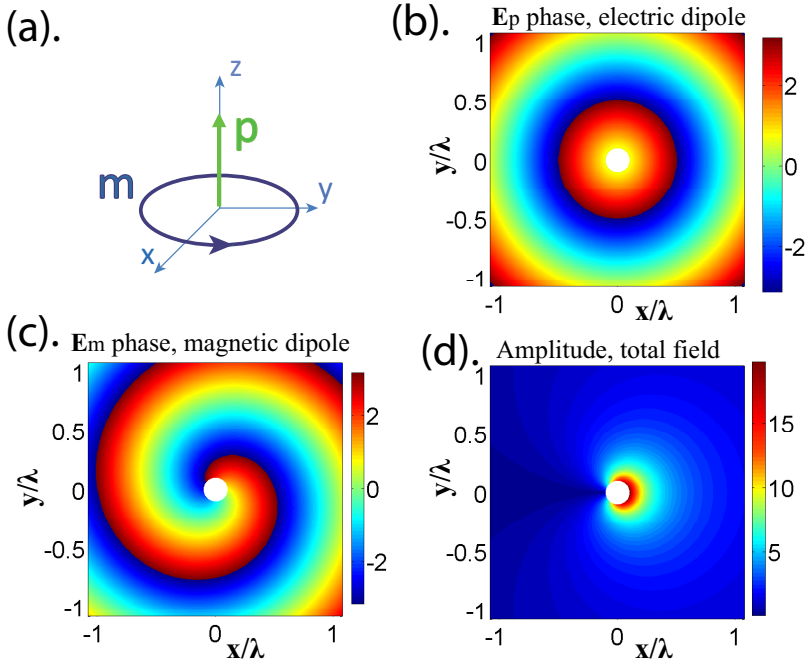


Figure 4.1: (a).Illustration of a spinning magnetic dipole \mathbf{m} in $z = 0$ plane and a electric dipole \mathbf{p} along z axis; (b).Radiation electric field in $z = 0$ plane of the electric dipole is cylindrically symmetric to the z axis; (c).Radiation electric field in $z = 0$ plane of the spinning magnetic dipole has a spiral phase; (d). Amplitude of the total electric field in $z = 0$ plane as a result of the two dipole interference.

symmetric around the z axis:

$$\mathbf{E}_p = \hat{\mathbf{z}} \frac{p_0 k^2}{\epsilon_0} \frac{e^{ikr}}{4\pi r} = \hat{\mathbf{z}} E_{zp} \frac{e^{ikr}}{4\pi r}, \quad (4.1)$$

whereas the farfield electric field in the $z = 0$ plane of the spinning magnetic dipole is also polarized along the z direction with a spiral phase:

$$\mathbf{E}_m = \hat{\mathbf{z}} (-i) m_0 k^2 Z_0 e^{i\phi} \frac{e^{ikr}}{4\pi r} = \hat{\mathbf{z}} E_{zm} e^{i\phi} \frac{e^{ikr}}{4\pi r}, \quad (4.2)$$

where (r, ϕ, θ) is the spherical coordinate, ϵ_0 is the vacuum permittivity, $Z_0 = 120\pi$ is the impedance of free space and $k = 2\pi/\lambda$ is the wavevector in air. If the magnetic and electric dipole are modulated in such a way that $E_{zp} = E_{zm} e^{i\phi_0}$, the total electric field in the xy plane is:

$$E_z = E_{zm} e^{i\phi_0} \frac{e^{ikr}}{4\pi r} + E_{zm} e^{i\phi} \frac{e^{ikr}}{4\pi r}. \quad (4.3)$$

As a result of the spiral phase of \mathbf{E}_m , the symmetry of the radiation field is broken and there is always a direction $\phi = \phi_0 + \pi$ where the destructive interference occurs. By changing the phase ϕ_0 of the electric dipole from 0 to 2π , the destructive interference

can be tuned to any direction in the $z = 0$ plane. This is different from the conventional Kerker's conditions where the unidirectionality can only be achieved in two directions when the linear electric and magnetic dipoles are in and out of phase.

4.3. DESIGNED EXCITATION WITH FOCUSED VECTOR VORTEX BEAMS

As is shown in the remaining of the chapter, the scattering direction of a high index dielectric nanosphere can be controlled by focusing an appropriate pupil field. Based on Mie's solution, the high-order multipole modes of a high index dielectric nanosphere are of narrow bandwidth. In this chapter, we will focus on the longer wavelength range where the electric and magnetic dipoles dominate and the higher order modes are negligible. In order to realize directional scattering with the proposed concept, one must excite the circularly polarized magnetic dipole in the $z = 0$ plane and the electric dipole in z direction and one must be able to control the amplitude and phase of these two dipoles separately. This, however, cannot be achieved with conventional plane wave illumination. In the current chapter, we utilize the unique focusing properties of designed pupil fields with unconventional polarization and phase distributions to independently generate a circularly polarized magnetic field and a linearly polarized electric field at the focal point.

As illustrated in Fig. 4.2(a), the proposed pupil field contains three annular rings in the amplitude function. The radius of the pupil is normalized to 1. Within each ring, the amplitude is uniform. For simplicity, all three rings are chosen to have narrow width. The electrical field in ring 1 with average radius ρ_1 and width $\Delta\rho_1 \ll 1$ is radially polarized: $\mathbf{E}_e = \mathbf{E}_1 = \hat{\rho} A_1 e^{i\phi_0}$, where ϕ_0 is a constant phase and A_1 is a positive real number. The focal fields can be calculated using the Richard Wolf diffraction integral [19, 20]. At the focal point $r_f = 0$ the focused electric field is longitudinally polarized along the z -direction and:

$$\begin{aligned} E_{f,z}^{rad}(r_f = 0) &= -2e^{i\phi_0} C_0 \int_0^1 A(\rho) \frac{s_0 \rho}{(1 - \rho^2 s_0^2)^{1/4}} \rho d\rho \\ &\approx -2e^{i\phi_0} C_0 A_1 \frac{s_0 \rho_1}{(1 - \rho_1^2 s_0^2)^{1/4}} \rho_1 \Delta\rho_1 \\ &= E_f e^{i\phi_0}, \end{aligned} \quad (4.4)$$

where s_0 is the numerical aperture and C_0 is a constant related to the wavelength, numerical aperture and focal length. This pupil field is used to excite the pure electric dipole of the dielectric nanosphere with the magnetic dipole mode completely suppressed [13].

The pupil field $\mathbf{E}_h = \mathbf{E}_2 + \mathbf{E}_3$ consists of two rings: ring 2 with average radius ρ_2 and width $\Delta\rho_2 \ll 1$ and ring 3 with average radius ρ_3 and width $\Delta\rho_3 \ll 1$, where $\rho_3 \ll \rho_2 < \rho_1$. The electric pupil fields in ring 2 and 3 are azimuthally polarized phase vortices: $\mathbf{E}_2 = \hat{\phi} A_2 e^{i\phi}$ and $\mathbf{E}_3 = -\alpha \mathbf{E}_2$, where α and A_2 are positive real numbers. The corresponding magnetic pupil field is a radially polarized phase vortex with $\mathbf{H}_h = \hat{\rho} / Z_0 |\mathbf{E}_h| e^{i\phi}$, where $Z_0 = 120\pi$. The corresponding fields at the focal point $r_f = 0$ can be calculated using Richard Wolf

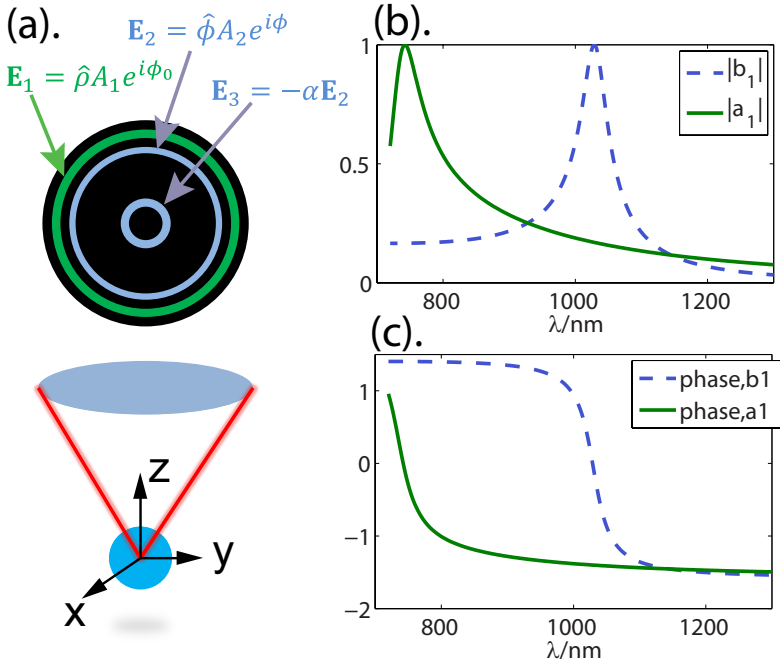


Figure 4.2: (a). Illustration of the configuration of focusing the pupil field to excite a high index dielectric sphere at focus; (b). Amplitude of the electric and magnetic scattering coefficients a_1 and b_1 as function of the wavelength for a high index dielectric sphere of refractive index $n = 5$ and radius $r_0 = 100$ nm; (c). Phase of a_1 and b_1 .

diffraction integral [19, 20]:

$$H_{f,x}^{azm,m=1} = \frac{C_0}{Z_0} \int_0^1 A(\rho)(1 - \rho^2 s_0^2)^{1/4} \rho d\rho \quad (4.5)$$

$$\approx \frac{C_0}{Z_0} [A_2(1 - \rho_2^2 s_0^2)^{1/4} \rho_2 \Delta\rho_2 - \alpha A_2(1 - \rho_3^2 s_0^2)^{1/4} \rho_3 \Delta\rho_3] = H_f,$$

$$H_{f,y}^{azm,m=1} = iH_{f,x}^{azm,m=1}(r_f = 0) = iH_f, \quad (4.6)$$

$$H_{f,z}^{azm,m=1} = 0, \quad (4.7)$$

$$\begin{aligned} E_{f,x}^{azm,m=1} &= iC_0 \int_0^1 A(\rho)(1 - \rho^2 s_0^2)^{-1/4} \rho d\rho \\ &\approx iC_0 \times \\ &\times [A_2(1 - \rho_2^2 s_0^2)^{-1/4} \rho_2 \Delta\rho_2 - \alpha A_2(1 - \rho_3^2 s_0^2)^{-1/4} \rho_3 \Delta\rho_3], \end{aligned} \quad (4.8)$$

$$E_{f,y}^{azm,m=1} = iE_{f,x}^{azm,m=1}, \quad (4.9)$$

$$E_{f,z}^{azm,m=1} = 0, \quad (4.10)$$

It follows from Eq. (4.5) to Eq. (4.10) that the transverse components of the focal magnetic field have $(1 - \rho^2 s_0^2)^{1/4}$ dependence in the diffraction integral while the transverse component of the focal electric field have $(1 - \rho^2 s_0^2)^{-1/4}$ dependence. When

$$\alpha = [(1 - \rho_2^2 s_0^2)^{-1/4} \rho_2 \Delta \rho_2] / [(1 - \rho_3^2 s_0^2)^{-1/4} \rho_3 \Delta \rho_3], \quad (4.11)$$

all the electrical field components become zero at the focal point, but the magnetic field $\mathbf{H}_f = H_f(\hat{\mathbf{x}} + i\hat{\mathbf{y}})$ is non-zero and circularly polarized, where

$$\begin{aligned} H_f &= \frac{C_0}{Z_0} A_2 (1 - \rho_2^2 s_0^2)^{-1/4} \rho_2 \Delta \rho_2 \times \\ &\times \left[\sqrt{1 - \rho_2^2 s_0^2} - \sqrt{1 - \rho_3^2 s_0^2} \right] \neq 0. \end{aligned} \quad (4.12)$$

In this way, a pure circularly polarized magnetic field at the focal point is created and the electric field vanishes there.

Note that the condition for α is independent of the wavelength. We remark that many other pupil fields can be designed to excite the electric and magnetic dipoles in the focal point. Indeed, the rings do not need to be narrow and by using broader rings, stronger dipole moments can be realized. However, the pupil field proposed in this chapter has the advantage of being particularly simple to illustrate the design principles. The realization of the proposed pupil fields would be possible with the recent demonstrations in the generation of arbitrary vector vortex beams using spatial light modulators [21] and q-plates [22, 23]. Specifically the generation of azimuthally/radially polarized phase vortices has been demonstrated recently using q-plates and spiral phase plate in [23].

It is shown in [13, 24] that electric dipole and magnetic dipole interactions of a given dielectric nanosphere illuminated by an inhomogeneous beam depend only on the local fields at the center of the sphere. When a high index dielectric nanosphere at focus is illuminated by the focal fields of the pupil field $\mathbf{E} = \mathbf{E}_h + \mathbf{E}_e$, within the wavelength range where the magnetic and electric dipole modes of the sphere dominate, a circularly polarized magnetic dipole $\mathbf{m} = i \frac{6\pi}{k^3} b_1 H_f (\hat{\mathbf{x}} + i\hat{\mathbf{y}})$ is excited with the pure contribution of pupil field \mathbf{E}_h while the linearly polarized electric dipole $\mathbf{p} = i \frac{6\pi}{k^3} \epsilon_0 a_1 E_f e^{i\phi_0} \hat{\mathbf{z}}$ is excited with the pure contribution of pupil field \mathbf{E}_e . Here a_1 and b_1 are the electric and magnetic dipole Mie scattering coefficients of a nanosphere, determined from the standard plane wave illumination [24]. Applying Eq. 4.1 and Eq. 4.2, in the $z = 0$ plane the total scattering field of the excited magnetic and electric dipole moments is:

$$\mathbf{E}_s = \hat{\mathbf{z}} \frac{6\pi}{k} (i a_1 E_f e^{i\phi_0} + b_1 Z_0 H_f e^{i\phi}) \frac{e^{ikr}}{4\pi r}. \quad (4.13)$$

This shows that when the focal fields follow the relation $120\pi |b_1 \mathbf{H}_f| = |a_1 \mathbf{E}_f|$ which is the amplitude requirement of the Kerker's condition for directional scattering [10], there is always a direction in the $z = 0$ plane where the phase condition for destructive interference $\phi = -\pi/2 + \phi_0 + \text{Arg}(a_1) - \text{Arg}(b_1)$ is fulfilled.

4.4. NUMERICAL VERIFICATIONS

The analytical model for angular tuning of the directional scattering is verified by a finite element method (FEM) simulation [25] of the scattering of a dielectric nanosphere

of refractive index 5 and radius 100 nm under the proposed excitation. The electric and magnetic dipole scattering coefficients a_1 and b_1 of the nanosphere are shown in Fig. 4.2(b) and (c). It is important to note that the same principle applies to practical high index nanospheres like Si/Ge with only different spectral dependences of the Mie coefficients a_1 and b_1 . Fig. 4.3(a) and Fig. 4.3(b) show the phases of the scattered electric fields in $z = 0$ plane of the nanoparticle excited respectively by the focusing pupil fields \mathbf{E}_h and \mathbf{E}_e . When the amplitude of \mathbf{E}_h and \mathbf{E}_e are modulated so that the focal fields satisfy the condition $120\pi|b_1\mathbf{H}_f| = |a_1\mathbf{E}_f|$, there is always a direction in $z = 0$ plane where the phase condition for directional scattering is fulfilled due to the spiral phase of the excited spinning magnetic dipole in Fig. 4.3(a) and the cylindrically symmetric phase of the excited longitudinal electric dipole in Fig. 4.3(b). As is shown in Fig. 4.3(c), when the amplitude requirement of Kerker's condition is satisfied for $\lambda = 1028$ nm, completely destructive interference is formed by these two scattering fields along the direction $\phi = -\pi/2 + \phi_0 + \text{Arg}(a_1) - \text{Arg}(b_1)$ in the $z = 0$ plane, and the directional scattering is thus achieved, clearly illustrated by the plot of the Poynting vector in Fig. 4.3(d).

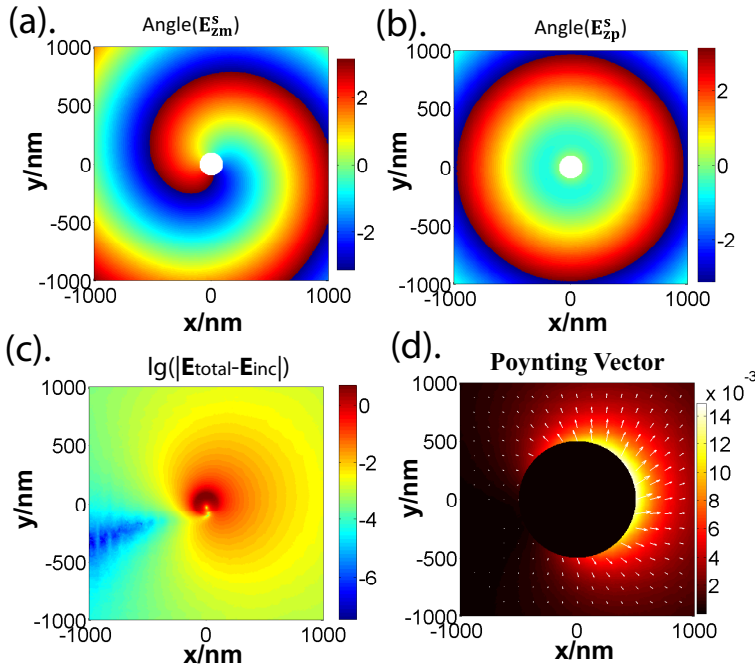


Figure 4.3: FEM simulations of the scattering of a sphere with radius 100 nm and refractive index 5 with the proposed excitation at wavelength $\lambda = 1028$ nm. (a).Phase of the scattered electric field in the $z = 0$ plane of the spinning magnetic dipole of the sphere excited by the focal field of \mathbf{E}_h ; (b).Phase of the scattering electric field in the $z = 0$ plane with the longitudinal electric dipole of the sphere excited by the focal field of \mathbf{E}_e ; (c). Amplitude of the total field subtracted by the incident field in logarithm scale in the $z = 0$ plane with both dipole excitations using pupil field $\mathbf{E}_h + \mathbf{E}_e$ when $120\pi|b_1\mathbf{H}_f| = |a_1\mathbf{E}_f|$ is fulfilled; (d). Poynting vector of the directional scattering (fields inside a circle with radius of 500 nm centered at the focal point is cropped to highlight the unidirectional scattering).

As shown in Fig. 4.4, by changing the phase ϕ_0 of the pupil field of $\mathbf{E}_e = \hat{\rho} A_1 e^{i\phi_0}$, the scattering can be tuned. When ϕ_0 is changed over 2π range, the scattering direction rotates over 2π range, making it possible to tune the scattering to any direction in the $z = 0$ plane by only modifying the phase of the radially polarized beam.

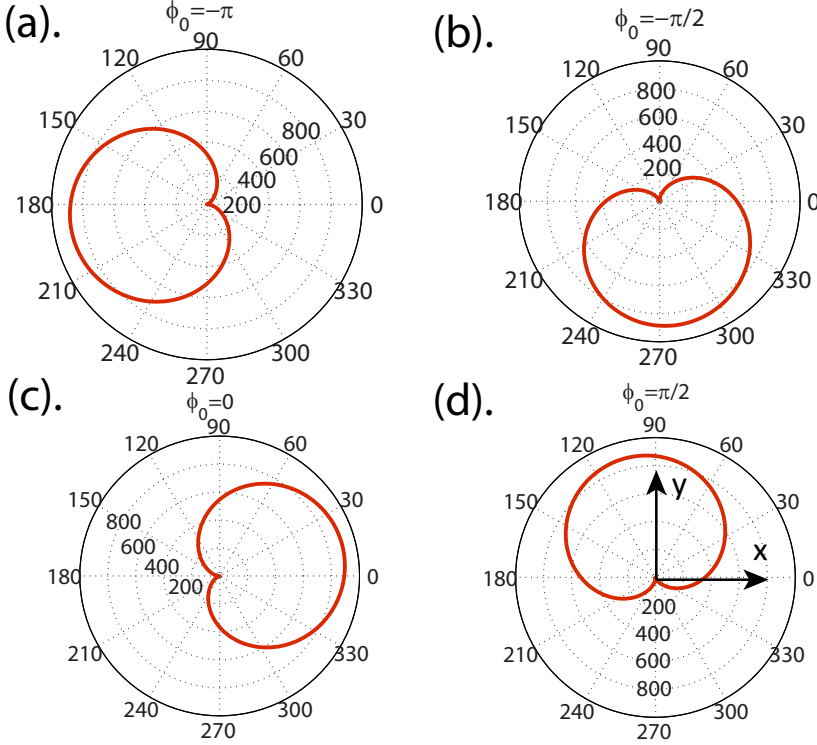


Figure 4.4: Angular tuning of the directional scattering shown by the scattering pattern when ϕ_0 is changed over 2π at $\lambda = 1028$ nm. (a). $\phi_0 = -\pi$; (b). $\phi_0 = -\pi/2$; (c). $\phi_0 = 0$; (d). $\phi_0 = \pi/2$.

Furthermore, this approach to control directional scattering works over a broad wavelength range as long as the dipole modes dominate and the higher orders are negligible. The directional scattering at different wavelengths can be fulfilled as shown in Fig. 4.5 with $120\pi|b_1 \mathbf{H}_f| = |a_1 \mathbf{E}_f|$ fulfilled by adjusting the amplitude of the pupil field \mathbf{E}_e and \mathbf{E}_h . From Fig. 4.5 and Fig. 4.4(c), one can see that when ϕ_0 is set to be zero, the direction where destructive interference happens changes at different wavelengths. However, the scattering at each wavelength can always be tuned to the desired direction by changing ϕ_0 as shown in Fig. 4.4.

Note that although we focus on the interference of a spinning magnetic dipole and a linearly polarized electric dipole, the directional scattering control can also be achieved with a spinning electric dipole and a linearly polarized magnetic dipole. The corresponding excitation focal field can be realized by applying an azimuthally polarized electric pupil field in ring 1 and adjusting α in ring 3 so that the magnetic field at focus is zero

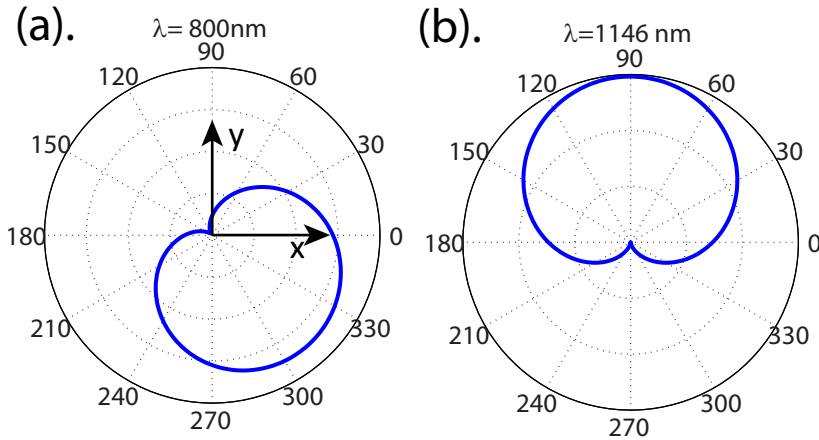


Figure 4.5: Scattering pattern at (a). $\lambda = 800 \text{ nm}$; (b). $\lambda = 1146 \text{ nm}$, $\phi_0 = 0$ for both wavelengths.

but the electric field is nonzero and circularly polarized.

4.5. CONCLUSION

In summary, we have proposed an approach to control the scattering direction of a high index dielectric nanosphere. This approach enables the simultaneous excitation and independent control of a circularly polarized magnetic and a linearly polarized electric dipole mode with the unique focusing properties of vector vortex beams. By simply adjusting the phase and amplitude of the pupil field, the directional scattering can be tuned to any direction in the selected plane and works over a relatively broad wavelength range. With this method, we introduce a new degree of freedom, namely angular tuning, of directional scattering. Our proposal has high potentials in many applications such as the light routing/switching on a photonic chip, quantum optical networks, directional emission of quantum emitters with designed excitation and optical metrology, etc.

REFERENCES

- [1] L. Wei, N. Bhattacharya and H.P. Urbach, *Adding a spin to kerker's condition: angular tuning of directional scattering with designed excitation*, Optics Lett. **42**, 1776 (2017).
- [2] F.J. Rodriguez-Fortuno, G Marino, P Ginzburg, D. O'Connor, A. Martinez, G.A. Wurtz and A.V. Zayats, *Near-field interference for the unidirectional excitation of electromagnetic guided modes*, Science **340**, 328 (2013).
- [3] Z Xi, Y Lu, W Yu, P Wang and H Ming, *Unidirectional surface plasmon launcher: rotating dipole mimicked by optical antennas*, J. Optics **16**, 105002 (2014).
- [4] Z. Xi, L. Wei, A.J.L. Adam, H.P. Urbach and L.P. Du, *Accurate feeding of nanoantenna by singular optics for nanoscale translational and rotational displacement sensing*, Phy. Rev. Letters **117**, 113903 (2016).
- [5] M Neugebauer, P Wozniak, A Bag, G Leuchs and P Banzer, *Polarization-controlled directional scattering for nanoscopic position sensing*, Nat. Communications **7**, 11286 (2016).
- [6] F.J. Rodriguez-Fortuno, N. Engheta, A. Martinez, and A.V. Zayats, *Lateral forces on circularly polarizable particles near a surface*, Nature Comm. **6**, 8799 (2015).
- [7] A.G. Curto, G. Volpe, T.H. Taminiau, M.P. Kreuzer, R. Quidant and N.F. van Hulst, *Unidirectional emission of a quantum dot coupled to a nanoantenna*, Science **329**, 930 (2010).
- [8] A.I. Kuznetsov, A.E. Miroshnichenko, Y.H. Fu, J.B. Zhang and B. Luk'yanchuk, *Magnetic light*, Sci. Reports **2**, 492 (2012).
- [9] A. Garcia-Etxarri, R. Gomez-Medina, L.S. Froufe-Perez, et al., *Strong magnetic response of submicron silicon particles in the infrared*, Opt. Express **19**, 4815 (2011).
- [10] Y.H. Fu, A.I. Kuznetsov, A.E. Miroshnichenko, Y.F. Yu and B. Luk'yanchuk, *Directional visible light scattering by silicon nanoparticles*, Nat. Communications **4**, 1527 (2012).
- [11] M. Kerker, G. Wang and G. Giles, *Electromagnetic scattering by magnetic spheres*, J. Opt. Soc. Am. **73**, 765 (1983).
- [12] X. Zambrana-Puyalto, I. Fernandez-Corbaton, M.L. Juan, X. Vidal and G. Molina-Terriza, *Duality symmetry and kerker conditions*, Optics Lett. **38**, 1857 (2013).
- [13] Z. Xi, L. Wei, A.J.L. Adam and H.P. Urbach, *Broadband active tuning of unidirectional scattering from nanoantenna using combined radially and azimuthally polarized beams*, Opt. Letters **41**, 33 (2016).
- [14] K.Y. Bliokh, F.J. Rodriguez-Fortuno, F. Nori and A.V. Zayats, *Spin-orbit interactions of light*, Nature Photonics **9**, 796 (2015).

- [15] D. O'Connor, P. Ginzburg, F.J. Rodriguez-Fortuno, G.A. Wurtz and A.V. Zayats, *Spin-orbit coupling in surface plasmon scattering by nanostructures*, Nat. Comm. **5**, 6327 (2014).
- [16] J. Petersen, J. Volz and A. Rauschenbeutel, *Chiral nanophotonic waveguide interface based on spin-orbit interaction of light*, Science **346**, 67 (2014).
- [17] J. Lin, J.P.B. Mueller, Q. Wang, G.H. Yuan, N. Antoniou, X.C. Yuan and F. Cappasso, *Chiral nanophotonic waveguide interface based on spin-orbit interaction of light*, Science **340**, 331 (2013).
- [18] D. Griffiths and R. College, *Introduction to Electrodynamics* (Prentice Hall, 1999).
- [19] B. Richards and E. Wolf, *Electromagnetic diffraction in optical systems ii. structure of the image field in an aplanatic system*, Proc. R. Soc. Lond. A **253**, 358 (1959).
- [20] L. Wei and H. Urbach, *Shaping the focal field of radially/azimuthally polarized phase vortex with zernike polynomials*, J. Optics **18**, 065608 (2016).
- [21] Z.Z. Chen, T.T. Zeng, B.J. Qian and J.P. Ding, *Complete shaping of optical vector beams*, Opt. Express **23**, 17701 (2015).
- [22] V. D'Ambrosio¹, F. Baccari, S. Slussarenko, L. Marrucci and F. Sciarrino, *Arbitrary, direct and deterministic manipulation of vector beams via electrically-tuned q-plates*, Sci. Reports **5**, 7840 (2015).
- [23] Z.X. Liu, Y.Y. Liu, Y.C. Liu, W.X. Shu, H.L. Luo and S.C. Wen, *Generation of arbitrarily vector vortex beams on hybrid order poincare sphere*, Photonics Research **5**, 15 (2017).
- [24] T. Das, P.P. Iyer and J.A. Schuller, *Beam engineering for selective and enhanced coupling to multipolar resonances*, Phys. Rev. B **92**, 241110 (2015).
- [25] X.H. Wei, A.J.H. Wachtters and H.P. Urbach, *Finite-element model for three-dimensional optical scattering problems*, J. Opt. Soc. Am. A **24**, 866 (2007).

5

SUSPENDED NANO-ANTENNA ARRAY

Due to the strong field enhancement at their plasmonic resonances, structured metallic nano-antenna arrays are used to improve the performance of surface enhanced infrared absorption (SEIRA) spectroscopy. The resonances of the nano-antenna arrays are strongly modified by the substrates that support them. We study suspended nano-antenna arrays that are supported by narrow silicon nano-pillars on planar silicon substrate. It is shown that the field enhancements of the suspended plasmonic nano-antenna arrays are dependent on the heights of the nano-pillars. There exists an optimum height of the nano-pillars at which the resonance electric fields of the nano-antenna's are considerably enhanced compared to when they are directly on the substrate. The resonant wavelengths of the suspended nano-antenna arrays are tuneable by varying incident angles of the illumination beams. A recipe for the fabrication of such nano-antenna array is also described.

5.1. INTRODUCTION

The ability to detect and distinguish trace molecules at an ultra-low concentration without the need for labeling is desirable and beneficial for many areas ranging from medical applications to industrial metrology. Surface plasmon resonance (SPR) sensors based on metallic thin films are mostly known for their high sensitivity in detecting refractive index changes. However, without labeling, they are not selective. Infrared absorption spectroscopy is a typical way to distinguish a mixture of molecules by measuring their vibrational spectrum, especially in the mid-infrared range. Different from metallic thin films that behave like perfect conductors in the mid-infrared, localized plasmon resonance (LPR) of metallic nano-antennas can be tailored to different wavelengths by changing their structural parameters. The strong field enhancement near the surface of the nanoparticles at LPR is demonstrated to enhance the sensitivity of infrared spectroscopy [1–3]. Due to the fact that the plasmonic resonance is strongly influenced by the refractive index surrounding the nano-antennas, the substrate on which the plasmonic nano-antennas are fabricated strongly affects the field enhancement. In this chapter, we study specifically the effect of the substrate and propose a design with suspended plasmonic nano-antenna array. A recipe for fabricating such suspended plasmonic nano-antenna array is also developed.

5.2. FLOATING NANO-ANTENNA ARRAY AND SILICON SUBSTRATE

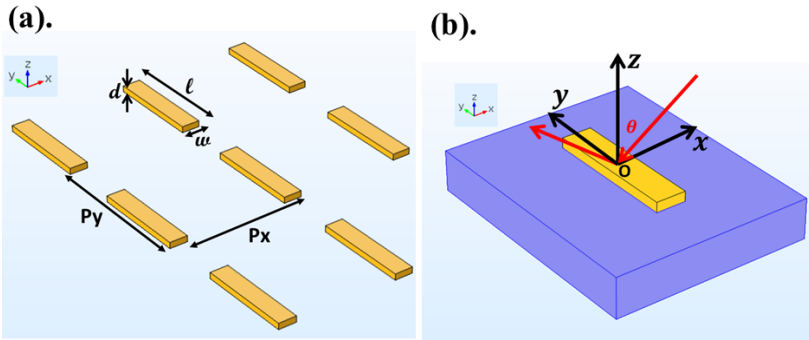


Figure 5.1: (a). Plasmonic nano-antenna array in vacuum with height d nm, length l , width w , pitch in x direction P_x and pitch in y direction P_y ; (b). Plasmonic nano-antenna array on substrate with the same parameters as (a), and θ is the incident angle.

The effect of the substrate on the plasmonic resonances can be illustrated by a direct comparison between a nano-antenna array floating in vacuum as in Fig. 5.1(a) and the same nano-antenna array on silicon substrate as in Fig. 5.1(b). The nano-antenna array is composed of gold dipole nano-antennas with height $d = 100$ nm, length $l = 1550$ nm, width $w = 300$ nm, pitch in x direction $P_x = 3000$ nm and pitch in y direction $P_y = 2500$ nm. The long axis of the nano-antenna is along the y direction, and the beam is incident in the $y = 0$ plane with TE polarization, i.e. the electric field is polarized parallel to the long axis of the dipole antenna. The permittivity of gold is obtained from the measure-

ments of evaporated gold by Olmon et al [4]. The refractive index of silicon is set to be 3.423. The single gold dipole antenna in vacuum has a resonance frequency at 4300 nm and the full-width-half-maxima (FWHM) is about 1 μm . The white dashed line in Fig. 5.2(a) denotes the (-1, 0) diffraction condition in air.

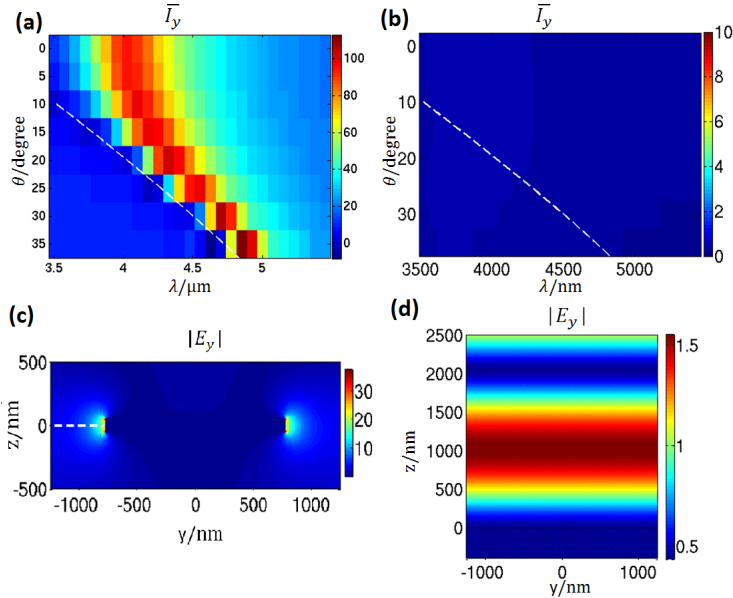


Figure 5.2: (a). Average intensity enhancement $\bar{I}_y = |E_y|^2$ along the white dashed line in Fig. 5.2(c) of the plasmonic nano-antenna array in vacuum with varying incident angles and wavelengths. The white dashed line in (a) denotes the (-1,0) diffraction order condition; (b). Average intensity enhancement \bar{I}_y the plasmonic nano-antenna array on Si substrate with varying incident angles and wavelengths. The white dashed line in (b) denotes the (-1,0) diffraction order condition; (c). Electric field amplitude $|E_y|$ distribution (normalized by incident electric field strength) of the nano-antenna in the $x = 0$ plane, where the incoming beam has a wavelength of 4.1 μm and the incidence angle is 0; (d). Inhomogeneous field distribution $|E_y|$ near the air/si interface (without nano-antenna array on the si substrate) due to the interference of the incoming and reflected electric fields.

In Fig. 5.2(a), we show the angular-spectral map of the field enhancement \bar{I}_y , which is the averaged intensity enhancement along the white dashed line in Fig. 5.2(c). The strong field enhancement near the (-1,0) diffraction order condition of the plasmonic dipole antenna array is a result of collective resonances mediated by diffractive coupling of localized plasmons [5, 6]. As can be seen from Fig. 5.2(a), the wavelength of maximum field enhancement can be tuned by changing the incident angle.

However, the making of floating nano-antenna array in practice is challenging. Most of the plasmonic nano-antenna are fabricated on a substrate, the effects of which have been studied extensively [7–9]. The substrate influences the resonances of the nano-antennas in various ways. First of all, the reflected field from the substrate forms an interference with the incoming field on the side where the nano-antenna resides. It is known that the scattering of a dipole nano-antenna depends strongly on the local interference field. As can be seen in Fig. 5.2(d), the interference field strength varies along

the z -axis. This implies a height dependence of the scattering field strength of the nano-antenna due to the interference between the incoming and reflected field from the substrate. Secondly, the plasmonic resonance of each nano-antenna depends strongly on the refractive index of the surroundings. A dielectric substrate is known to bring a red shift of the plasmonic resonances [8]. As can be seen in Fig. 5.2(b), no field enhancement is visible within the region of interest when putting the same nano-antenna array as in Fig. 5.2(a) on a high index dielectric substrate. Last but not least, the scattering of nano-antenna can be considered equivalently as the radiation of an electric dipole above a planar interface. This important issue has been studied by W. Lukosz et al [10], where it is shown that the lifetime of the dipole depends on its distance to the substrate. This implies that the scattering of a dipole nano-antenna is strongly related to the substrate and its distance to the substrate. Based on above considerations, we will focus in this chapter on the substrate effects, especially the influences of the distance of the nano-antenna array to the substrate. Because the fabrication process of silicon is mature, we will concentrate in this chapter on the silicon substrate. A recipe is introduced to fabricate the proposed plasmonic nano-antenna array with which the distance of the nano-antenna array to the substrate can be precisely controlled.

5

5.3. SUSPENDED NANO-ANTENNA ARRAY

In this section, we propose a nano-antenna array suspended and supported by narrow Si pillars of height h as illustrated in Fig. 5.3 and investigate the height h dependence of the field enhancement.

In Fig. 5.4(a), we consider the influence of the height h on the strength of the field en-

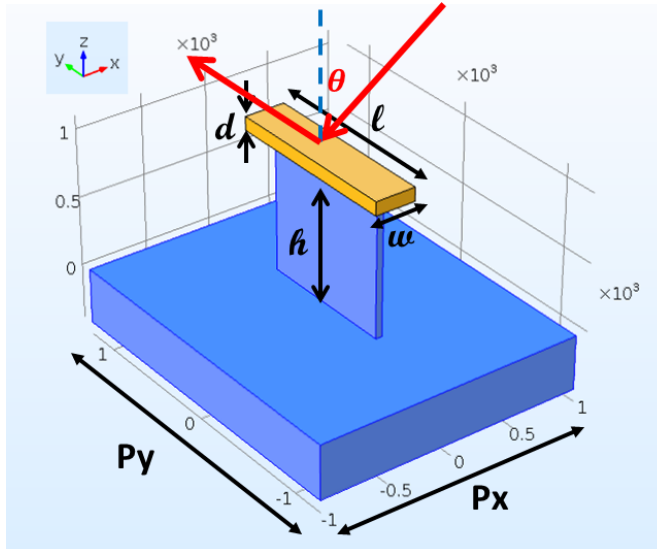


Figure 5.3: A suspended gold nano-antenna array supported by Si pillars.

hancement as well as its spectral distributions. The gold nano-antenna array has exactly

the same configuration as in Fig. 5.1(a) but now supported by Si pillars of width 50 nm, length 1300 nm and height h . The average intensity enhancements \bar{I}_y along a cut line connecting the points $(0, -(P_y + l)/2, h + d/2)$ and $(0, -P_y/2, h + d/2)$ are shown in Fig. 5.4(a). The nano-antenna array is illuminated by oblique incident plane wave at an angle of 20 degree and the white dashed line in Fig. 5.4(a) indicates the condition of the (-1, 0) diffraction order. As can be shown from Fig. 5.4(a), the enhancement of the nano-antenna array is very weak when its distance to the silicon substrate is below 500 nm. A clear tendency of red shift of the field enhancement spectrum is visible as the nano-antenna array gets closer to the Si substrate. In Fig. 5.4(b), Fig. 5.4(c) and Fig. 5.4(d), the angular-spectral maps of the intensity enhancements are shown where the nano-antenna arrays are located at three different distances to the substrate, respectively 250 nm, 1000 nm and 1650 nm. The white dashed lines, as in Fig. 5.4(a), represent the condition of the (-1, 0) diffraction order. Fig. 5.4(b), Fig. 5.4(c) and Fig. 5.4(d) confirm again that the redshift and degradation of the enhancements when the nano-antenna array is in close vicinity to the silicon substrate. This is especially true for smaller incident angles where no wavelength between 3500 nm to 5500 nm meets the condition of the (-1, 0) diffraction order. Comparing Fig. 5.2(a) and Fig. 5.4(d), the highly lifted nano-antenna array with a distance of 1650 nm to the substrate reproduces pretty well the angular-spectral map of the intensity enhancement of the antenna array floating in vacuum. This means the proposed suspended nano-antenna array provides a practical way to realize the optical properties of the floating nano-antenna array. Compared to the nano-antenna array directly fabricated on high index substrate, the enhancement is not only much higher but also accessible on both the top and bottom side of the nano-antenna. This generates a relatively higher interaction volume. From Fig. 5.4(d), we can also see that the maximum enhancement wavelength can be tuned over a relative broad range over 800 nm by changing the incident angle from 0 to 35 degree. This spectral tune-ability by changing incident angle can be explained by the Rayleigh anomaly which also occurs in the floating nano-antenna array in Fig. 5.2(a).

The material of the substrate itself will of course have an impact on the nano-antenna array. As a comparison, we keep all the parameters of the nano-antenna array and its supporting nano-pillars the same but change the substrate to gold as illustrated in the inset of Fig. 5.5(a). As is shown in Fig. 5.5, the dependences of the nano-antenna array's field enhancement on the nano-pillar's height h , incident angle and wavelength are distinctively different on the gold substrate from on the silicon substrate in Fig. 5.4. First of all, the maximum average intensity enhancement is reached at a height much nearer to the surface of the gold substrate as can be seen from Fig. 5.5(c). At the optimum height for field enhancement $h = 250$ nm, as we can see from Fig. 5.5(a), however, the angular-spectral map for the field enhancement of the nano-antenna array on the gold substrate deviates quite a lot from the floating nano-antenna in Fig. 5.2(a) and the nanoantenna on Si substrate in Fig. 5.5(d). The maximum enhancement wavelength is strongly red-shifted. By comparing it with the nano-antenna array supported by virtual 'air' nano-pillars above the gold substrate in Fig. 5.5(d), we can see that this red-shift is caused mainly by the supporting high index Si nano-pillars. This can also be understood by comparing the near-field electric energy distributions of the nano-antenna arrays on Si substrate in Fig. 5.7(a) and on Au substrate in Fig. 5.7(b), where both are under its op-

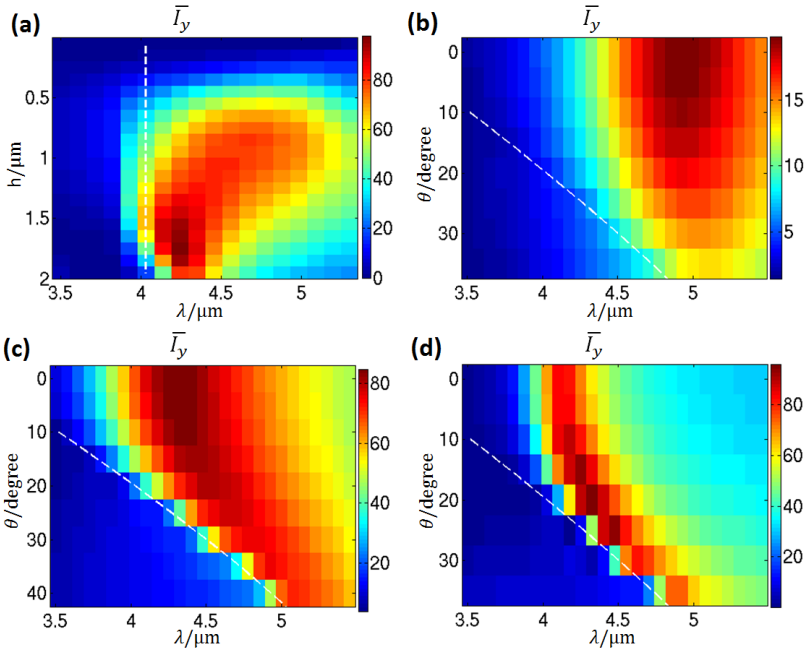


Figure 5.4: (a). Average intensity enhancement \bar{I}_y of the suspended plasmonic nano-antenna array at varying heights of the supporting Si pillars and wavelengths of the illumination. The incoming beam is TE polarized and incident in the xz plane with an incident angle of 20 degree; The angular-spectral map of the intensity enhancement at $h = 250$ nm; (c) The angular-spectral map of the intensity enhancement at $h = 1000$ nm; (d) The angular-spectral map of the intensity enhancement at $h = 1650$ nm. The white dashed line in denotes the $(-1,0)$ diffraction order.

timum configuration for the field enhancement. We can see that the fields inside the Si nano-pillars are much stronger in the case of a gold substrate and lower height h , while the fields inside the Si nano-pillars are negligible in the case of a Si substrate and higher h . Another observation from Fig. 5.5 is that the maximum enhancement achievable on gold substrates is much higher than on Si substrate. Even at a higher $h = 1000$ nm which is not the optimum for field enhancement, it still reaches similar enhancement strength on the gold substrate as the optimum enhancement strength on the Si substrate and over a wider range of incident angles and wavelengths.

In order to further understand the differences between gold and dielectric silicon substrates, we calculate the averaged intensity enhancement of a single gold antenna with a supporting Si nano-pillar of varying height on the Si and Au substrate as shown in Fig. 5.6(a). This is then compared to the normalised lifetime in Fig. 5.6(b) of a radiating horizontal electric dipole of varying height above the substrate, following the analytical formalism in chapter 10 of Ref. [11]. It can be seen that the local field enhancement near the nano-antenna follows similar height dependence to the two different type of substrates as the normalised lifetime of a horizontal electric dipole. From Fig. 5.6(a), we can see that the maximum field enhancement around the nano-antenna is much stronger

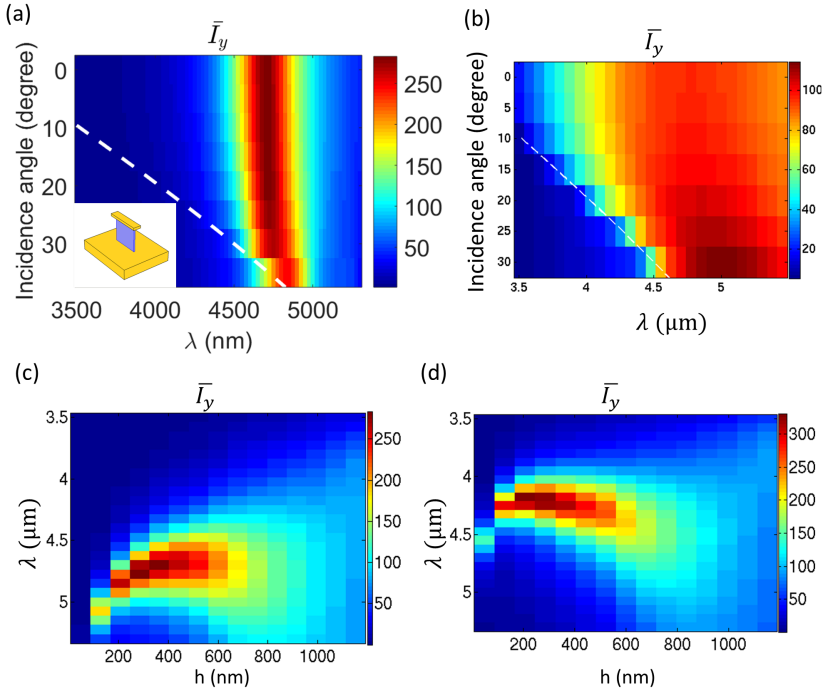


Figure 5.5: The angular-spectral map of the average intensity enhancement \bar{I}_y of the gold nano-antenna array supported by Si nano-pillars on gold substrate (as illustrated in the inset of (a)) at (a) $h = 250$ nm and (b) $h = 1000$ nm. Both are illuminated with TE polarised beams incident in the xz plane, and the white dashed line denotes the $(-1, 0)$ diffraction order condition. (c) The averaged intensity enhancement \bar{I}_y of the nano-antenna array with varying heights h of the supporting Si nano-pillars and varying wavelengths of light incident TE polarised in the xz plane at normal incidence. (d) The averaged intensity enhancement \bar{I}_y of the nano-antenna array with varying heights h of 'air' nano-pillars (i.e. floating antenna) above the gold substrate and varying wavelengths of light incident TE polarised in the xz plane at normal incidence.

when it is on a gold substrate and this is achieved at a lower h height than on a Si substrate. Similar behaviour can be found in Fig. 5.6(b): the maximum radiation lifetime of the horizontal electric dipole is much longer on a gold substrate than on the Si substrate, and this maximum lifetime is achieved much nearer to the gold substrate than to the Si substrate. For the height within a quarter of the wavelengths, gold substrates generally support longer lifetime (lower spontaneous decay rate) of the horizontal electric dipole and higher averaged field enhancement near the dipole nano-antenna. This simple physical model of the interaction between the single dipole with substrates gives us a clearer image why the angular-spectrum map of the field enhancement of the nano-antenna arrays are so different on a Si substrate in Fig. 5.4 from on a gold substrate in Fig. 5.5.

It is important to bear in mind that though the field enhancement can be very large with the designed plasmonic nano-antenna array, it is mainly suitable for small interaction volume and surface based detection geometries. First of all, volumes of strong field enhancement arising from the LPR of metallic nanoparticles are extremely small, of the

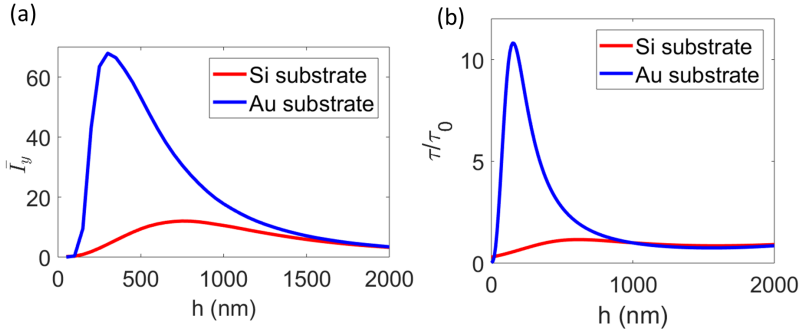


Figure 5.6: (a). The averaged intensity enhancement \bar{I}_y of a single gold nano-antenna with supporting silicon nano-pillar of vary heights h on the Si and Au substrate. The nano-antenna is illuminated by a TE polarised beam incident in the xz plane at the wavelength 4700 nm and normal incidence. (b). The normalised lifetime (normalised to the lifetime of a dipole in free space) of a horizontal electric dipole with varying heights to the Si and Au substrate. The wavelength is set to be 4700 nm.

order of $\text{sub-}\mu\text{m}^3$, as can be seen in Fig. 5.7(a) and Fig. 5.7(b). This may be useful for single molecule or molecular monolayer analysis when the molecules are already positioned in the region of the field 'hotspot'. In the case of detection of ultra-low concentration molecules in gas phases this technique is not very useful [12] since the interaction volume is limited as compared to conventional laser spectroscopy with multi-pass cavities [13] that allows extremely long effective path length. The main technical challenge in trying to use the present technique for gas phase would be to efficiently direct the target molecules to the 'hotspot' [14]. Clever vacuum technology would have to be used as in case of fiber based [15] gas detection schemes. But for surface based schemes like conventional ATR as used in industry, we need to take into account both the strong field enhancement as well as the small interaction volume of the nano-antenna.

In order to make a reasonable comparison with the conventional ATR configuration used in industry, we need to take into account both the strong field enhancement as well as the small interaction volume of the nano-antenna. In doing so, we calculate the total electric energy within a single unit cell area of the nano-antenna array in the xy plane directly above the top surface of the array as shown in Fig. 5.7(d). We then compare it with the total electric energy within the same unit cell area in the xy plane directly above the Si surface in the case of ATR with the same incident beam intensity as shown in Fig. 5.7(c). As is illustrated in the inset figure of Fig. 5.7(c), the ATR configuration consists of a bulky Si hemisphere with incident IR light illuminated from air at an angle $\theta = 60$ degree. For the nano-antenna array above the gold substrate under the optimum condition as in Fig. 5.7(b), about 100 times higher electric energy can be achieved compared to ATR, which is about 60 times higher than a beam of same incident intensity propagating in free space through the same unit cell area. For the array on Si substrate under its optimum condition as in Fig. 5.7(a), still 40 times stronger enhancement can be achieved than ATR. This large field enhancement taking into account the interaction volume proves that the proposed configuration could be beneficial for applications like the spectroscopic signals enhancement of molecular monolayers as well as enhanced

photocurrent generation[16].

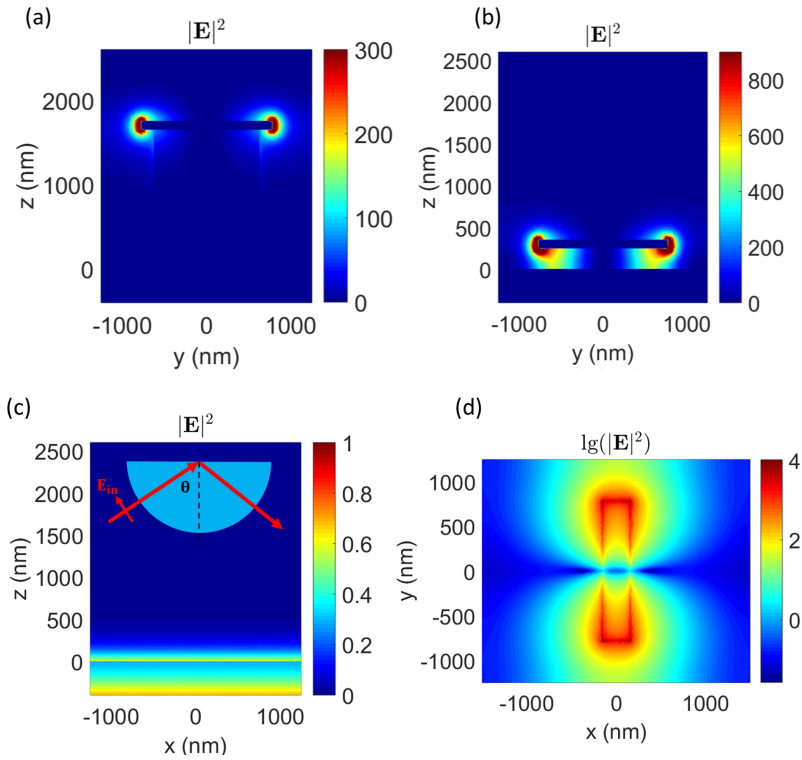


Figure 5.7: (a) The electric energy density in the yz cross section of the nano-antenna array supported by Si nano-pillars with height $h = 1650$ nm to the Si substrate, the illumination light is incident in the xz plane from the air side and is TE polarised at wavelength 4325 nm and incident angle 20 degree. (b) The electric energy density in the yz plane of the nano-antenna array supported by Si nano-pillars with height $h = 250$ nm to the Au substrate, the illumination light is incident in the xz plane from the air side and is TE polarised at wavelength 4700 nm and incident angle 0 degree; (c) ATR at the Si-air interface, the illumination light is incident, TM polarised, in the xz plane from Si side at wavelength 4700 nm and incident angle 60 degree with the same power as in (b); (d) The electric energy density of a unit cell of the array in logarithm scale in the xy plane at 10 nm high above the top surface of the nano-antenna array on gold substrate. All the parameters are the same as in (b).

5.4. NANO-FABRICATION OF THE SUSPENDED NANO-ANTENNA ARRAY

In this session, we describe the recipe to fabricate such suspended nano-antenna array which we developed in the Kavli Nanolab in Delft. As is illustrated in Fig. 5.8, the recipe consists of 8 steps:

1. Spin coat 350 nm e-beam resist CSAR 62 [17] on a clean 19 mm × 19 mm silicon substrate. The resist is then baked on hot plate at 150°C for 3 min;
2. The nano-antenna array is patterned on the resist using the Raith EBPG5200 e-beam lithography system with an e-beam dose of 310 $\mu\text{C}/\text{cm}^2$ and beam current at 2.25 nA. The exposed patterns are removed by a development procedure first in pentyl acetate for 50s at 19°C followed by rinsing 60s with IPA and N_2 drying;
3. The TEMESCAL e-beam deposition system is used to deposit an adhesion layer of 5 nm Ti (deposition rate 0.5 $\text{\AA}/\text{s}$) followed by a 100 nm Au (deposition rate 1.5 $\text{\AA}/\text{s}$) and 30nm Cr (deposition rate 1 $\text{\AA}/\text{s}$, the Cr layer serves as a protection layer to avoid sputtering etch of Au in later RIE procedure 5.);
4. The gold nano-antenna array on silicon is generated by the lift-off of the CSAR 62 resist in acetone first at a temperature of 50°C and then assisted by ultrasound;
5. Reactive ion etching of Si using a combination of etching gas 11.5 sccm SF_6 , 2.4 sccm O_2 and 10 sccm He with pressure of 7 μbar . The RF power is kept at 22 W. This results in an etch rate of Si around 58 nm/min;
6. Another layer of 30 nm Cr (deposition rate 1 $\text{\AA}/\text{s}$) is deposited using the TEMSCAL machine;
7. Reactive ion etching of Si using a combination of etching gas 13.75 sccm SF_6 , 2.2 sccm O_2 and 10 sccm He at a pressure of 13 μbar . The RF power is kept at 35 W. This step is performed to make the Si support pillar thinner;
8. At the final step, the Cr protection layer is removed by wet etching using Cr etchant.

The quality of the samples fabricated using this recipe are investigated using a scanning electron microscope (SEM). The gold nano-antenna array after the liftoff in recipe step 4 and first RIE in recipe step 5 are shown respectively in Fig. 5.9(a) and Fig. 5.9(b). The final suspended nano-antenna array are shown in Fig. 5.9(c) and Fig. 5.9(d), where it can be seen that the proposed design in Fig. 5.3 has been realized with the recipe developed.

5.5. CONCLUSION

In this chapter, we study the suspended nano-antenna arrays that are supported by narrow silicon nano-pillars on planar silicon substrate to enable large field enhancement in the infrared with the ultimate goal to improve the performance of surface enhanced infrared spectroscopy. We show that the field enhancements of the suspended plasmonic

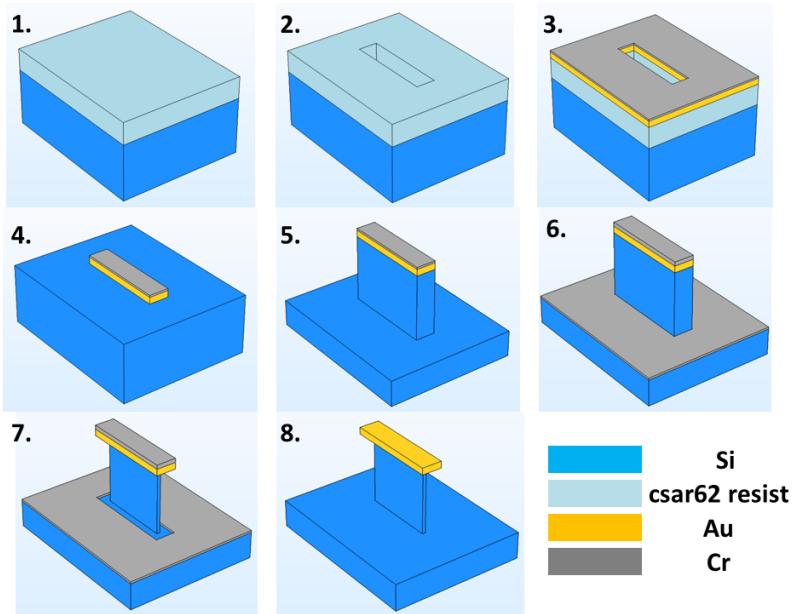


Figure 5.8: Nano-fabrication of suspended gold antenna array on Si substrate: 1. spin coat E-beam resist; 2. E-beam patterning and development; 3. Thin deposition of 100 nm Au and 20 nm Cr; 4. lift-off; 5. Reactive ion etching (RIE) of Si; 6. deposition of 30 nm Cr; 7. RIE of Si; 8. Removal of Cr with Cr etchant.

nano-antenna arrays are dependent on the heights of the nano-pillars. There exists an optimum height at which the nano-antenna's electric fields at resonance are enhanced considerably compared to when the antennas are situated directly on the substrate. The resonant wavelengths of the suspended nano-antenna arrays are tunable within a relative broad wavelength range up to $1 \mu\text{m}$ by changing the incident angle of the illumination beam. Further parameter optimization like adjustment of the pitch of the array can further improve the enhancement. A recipe for the fabrication of such nano-antenna array is also developed. The study in this chapter serves as the design and fabrication principles for future surface enhanced infrared spectroscopy.

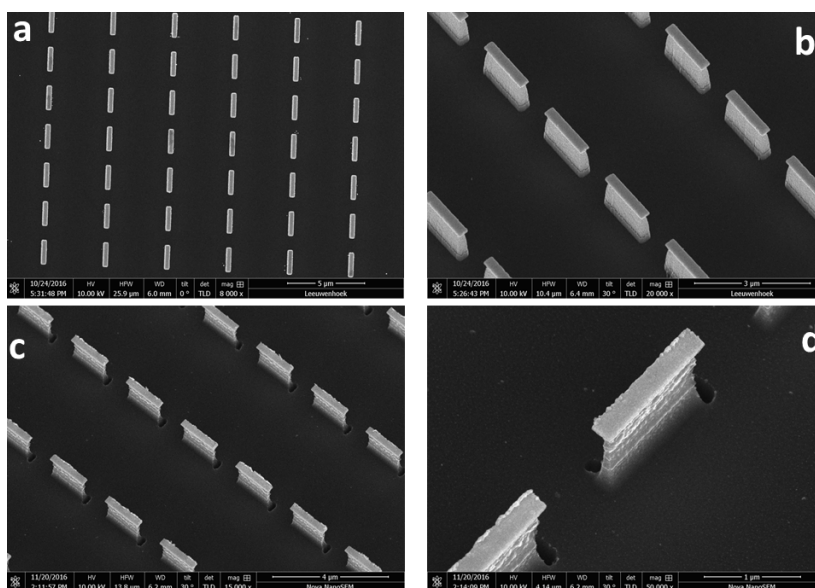


Figure 5.9: SEM image of the nano-antenna array. (a) after the lift off procedure; (b). After recipe step 5, RIE etching of Si; (c) and (d) Suspended nano-antenna array after recipe step 8.

REFERENCES

- [1] F. Neubrech, C. Huck, K. Weber, A. Pucci and H. Giessen, *Surface-enhanced infrared spectroscopy using resonant nanoantennas*, *Chemical Reviews* **117**, 5110 (2017).
- [2] C. Huck, A. Toma, F. Neubrech, M. Chirumamilla, J. Vogt, F. De Angelis and A. Pucci, *Gold nanoantennas on a pedestal for plasmonic enhancement in the infrared*, *ACS Photonics* **2**, 497 (2015).
- [3] R. Adato, S. Aksu and H. Altug, *Engineering mid-infrared nanoantennas for surface enhanced infrared absorption spectroscopy*, *Materials Today* **18**, 436 (2015).
- [4] R.L. Olmon, B. Slovick, T.W. Johnson, D. Shelton, S.H. Oh, G.D. Boreman and M.B. Raschke, *Optical dielectric function of gold*, *Phys. Rev. B* **86**, 235147 (2012).
- [5] K.T. Carron, W. Fluhr, M. Meier, A. Wokaun and H.W. Lehmann, *Resonances of two-dimensional particle gratings in surface-enhanced raman scattering*, *J. Opt. Soc. Am. B* **3**, 430 (1986).
- [6] T.W.W. Mab and T. Taubner, *Incident angle-tuning of infrared antenna array resonances for molecular sensing*, *ACS Photonics* **2**, 1498 (2015).
- [7] J. Lerme, C. Bonnet, M. Broyer, E. Cottancin, D. Manchon and M. Pellarin, *Optical properties of a particle above a dielectric interface: Cross sections, benchmark calculations, and analysis of the intrinsic substrate effects*, *J. Phys. Chem. C* **117**, 6383 (2013).

- [8] M.W. Knight, Y.P. Wu, J.B. Lassiter, P. Nordlander and N.J. Halas, *Substrates matter: Influence of an adjacent dielectric on an individual plasmonic nanoparticle*, Nano Letters **9**, 2188 (2009).
- [9] A.L. Holsteen, S. Raza, P. Fan, P.G. Kik, M.L. Brongersma, *Purcell effect for active tuning of light scattering from semiconductor optical antennas*, Science **358**, 1407 (2017).
- [10] W. Lukosz and R.E. Kunz, *Light emission by magnetic and electric dipoles close to a plane interface. i. total radiated power*, J. Opt. Soc. Am. **67**, 1607 (1977).
- [11] L. Novotny and B. Hecht, *Principles of nano-optics* (Cambridge university press, 2012).
- [12] A.B. Dahlin, *Size matters: problems and advantages associated with highly miniaturized sensors*, Sensors **12**, 3018 (2012).
- [13] F. Adler, P. Maslowski, A. Foltynowicz, K.C. Cossel, T.C. Briles, I. Hartl and J. Ye, *Mid-infrared fourier transform spectroscopy with a broadband frequency comb*, Optics Express **18**, 21861 (2010).
- [14] T.M. Squires, R.J. Messinger and S.R. Manalis, *Making it stick: convection, reaction and diffusion in surface-based biosensors*, Nature biotech. **26**, 417 (2008).
- [15] W. Jin, H.J. Ho, Y.C. Cao, J. Ju and L.F. Qi, *Gas detection with micro- and nano-engineered optical fibers*, Optical Fiber Technology **19**, 741 (2013).
- [16] C. H. Liu, Y. C. Chang, T. B. Norris, and Z. Zhong, *Graphene photodetectors with ultra-broadband and high responsivity at room temperature*, Nature Nanotechnology **9**, 273 (2014).
- [17] Csar 62 (ar-p 6200), <http://www.allresist.com/csar-62-ar-p-6200/>, accessed: 2017-05-08.

6

OUTLOOK

In this thesis, we first study the unique focusing properties of vector vortex beams and how complex field topologies can be designed by engineering the field on the exit pupil. As the main results of this thesis show, studying the interaction of structured light at focus and structured matter not only gives us better understanding to basic physics like non-radiating current sources but also enables new concepts for applications such as directional light coupling. Yet, structured light and matter interactions have much broader implications than what we are able to cover, some ideas are not fully explored at the time of drafting this thesis and may be considered as suggestions for future research:

1. Nonlinearity of dielectric nanoparticles at focus:

Compared to lossy metallic nanostructures, high index dielectric nanoparticles made of silicon or germanium have much lower absorption coefficients in the infrared wavelength range and suffer from much less absorption to sustain high power illuminations. Also, those nanoparticles have very strong internal fields at multipolar resonances and relatively large mode volume compared to the metallic counterparts, making them nice candidates for studying nonlinear optical phenomena [1]. The selective excitations of the multipole modes with the designed vector vortex beams imply a way to control the radiation patterns[2] of the nonlinear emission and improve the efficiency of such nonlinear conversions. On the other hand, the nonlinear properties like third harmonic generation of high index dielectric nanoparticles[3] provide a way to experimentally demonstrate our proposal on the excitation of 'ideal' radiationless anapole moment. The scattering of the nanoparticle can be completely suppressed at the anapole condition, while the induced current can be demonstrated by the enhanced nonlinear emission due to relatively strong internal electric fields.

2. Directionality for integrated optics and metrology:

In Chapter 4, we present the concept and a proof of principle study of angular tuning of directional scattering based on the excitation and interference of a longitudinal electric and a spinning magnetic dipole of a dielectric nanosphere. It will

be interesting to investigate how such concept can be realized for the directional coupling of light to waveguides on integrated photonic chips[4]. Whether angular tuning still works when high order multipole modes are included to achieve better directivity is subject to further investigation.

As shown in Chapter 4, the uni-directional scattering condition is fulfilled when $120\pi|b_1\mathbf{H}_f| = |a_1\mathbf{E}_f|$, and the direction where complete destructive interference occurs is along $\phi = -\pi/2 + \phi_0 + \text{Arg}(a_1) - \text{Arg}(b_1)$. Adjusting $|\mathbf{E}_f|$ and $|\mathbf{H}_f|$ by modifying the pupil field strength until the uni-directional scattering appears gives information about $|a_1/b_1|$, while the direction tells the phase difference between the two $\text{Arg}(a_1) - \text{Arg}(b_1)$. Though preliminary, this shows some potential to use the directivity measurement to retrieve the parameters like the dipole coefficients of the nanoparticles.

3. FTIR measurements of the nano-antenna array:

At the end of the project, to characterize the nano-antenna array, we were able to access and modify the commercial Fourier Transform Infrared (FTIR) Spectroscopy setup Bruker tensor 37 in Philips Innovation Services in Eindhoven. The FTIR setup has a broadband thermal lamp source covering the mid-infrared wavelength range and a liquid nitrogen cooled HgCdTe detector from InfraRed associates which has a detection window between $2\ \mu\text{m}$ and $5\ \mu\text{m}$. An accessory designed for the experiment is illustrated in Fig. 6.1(a). This accessory was built as shown in Fig. 6.1(b) to measure the incident angle-dependent reflection spectrum of the plasmonic nano-antenna array designed in chapter 5. The incident angle $\theta = \tan^{-1}(\frac{x_0}{z_0})$ can be tuned by translating the mirrors M1 and M2 to change x_0 symmetrically to the plane $x = 0$. During the translation, the M1 and M2 mirrors are rotated to make sure the beam hit the center of the nano-antenna array sample. The design of angle adjustment in Fig. 5 has the advantages of simplicity and cost effectiveness. However, the alignment of the optical path turns out to be challenging. This is mainly due the fact that the accessory was realized on a Thorlabs breadboard of length 250 mm and width 200 mm in order to fit the accessory in the limited space of the Bruker tensor 37 FTIR setup. The precision in determining of the incident angle is strongly influenced by the alignment while changing the angles by translating and rotating mirrors M1 and M2. A stepper motor (as used in optical ellipsometers) is recommended to gain high precision angular tuning but it requires an open bulky system instead of the closed commercial FTIR setup.

As we learn from chapter 5, the field enhancement of the nano-antenna array strongly depends on the incident angle. Thus this accessory still needs some more optimisation so that the actual angle of incidence can be tuned and determined precisely to measure the angular-spectral properties of the nano-antenna array. Several iterations have to be made to check the design and quality of the nano-antenna array with the accessory, then refine the fabrication in the cleanroom based on the feedback from the FTIR measurements. Though we have developed the fabrication recipe for the suspended nano-antenna array in chapter 5, the whole fabrication includes a few heavily occupied machines (EBPG, TEMESCAL thin film deposition and Leybold F1 reactive ion etching) in the cleanroom and it

takes a long time to complete the refinement feedback loop of fabrications, FTIR measurements, analysis and fabrication. At the moment of submission of this thesis it was not possible to obtain measurements of sufficient quality to be included in the thesis. The complete design of the accessory and the developed fabrication recipe of the nano-antenna array is available for the future continuation of this work.

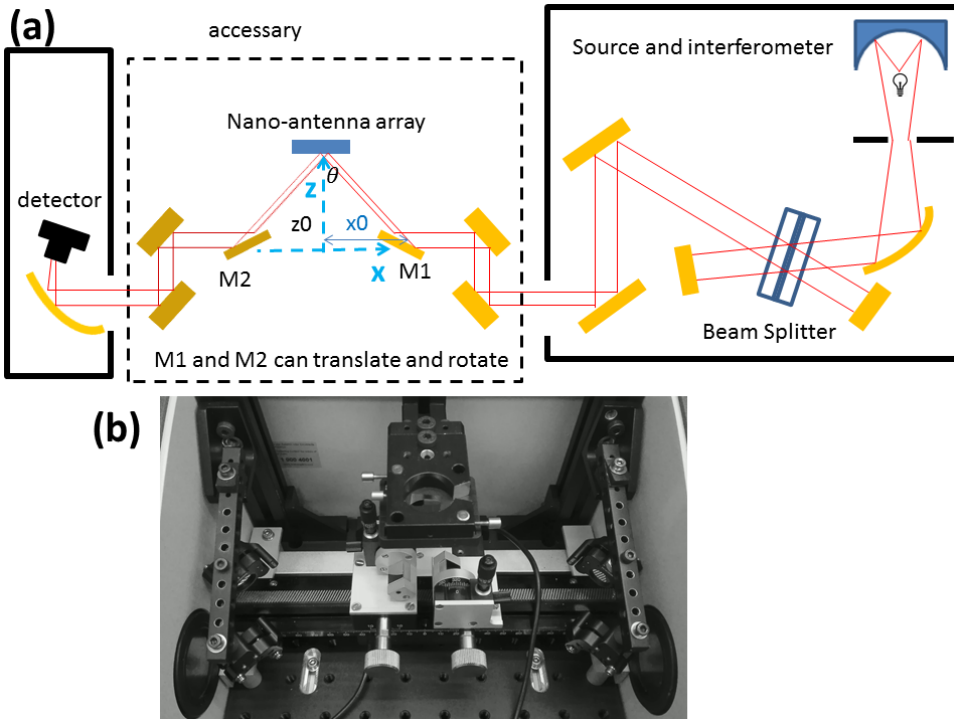


Figure 6.1: (a). Illustration of the FTIR setup and an accessory module to measure the angle-dependent spectrum of the nano-antenna array; (b). The actual accessory.

REFERENCES

- [1] D. Smirnova and Y.S. Kivshar, *Multipolar nonlinear nanophotonics*, *Optica* **3**, 1241 (2016).
- [2] L. Carletti, A. Locatelli, D. Neshev and C. De Angelis, *Shaping the radiation pattern of second harmonic generation from AlGaAs dielectric nanoantennas*, *ACS Photonics* **3**, 1500 (2016).
- [3] G. Grinblat, Y. Li, M.P. Nielsen, R.F. Oulton and S.A. Maier, *Enhanced third harmonic generation in single germanium nanodisks excited at the anapole mode*, *Nano Letters* **7**, 4635 (2016).
- [4] F.J. Rodriguez-Fortuno, G Marino, P Ginzburg, D. O'Connor, A. Martinez, G.A. Wurtz and A.V. Zayats, *Near-field interference for the unidirectional excitation of electromagnetic guided modes*, *Science* **340**, 328 (2013).

ACKNOWLEDGEMENTS

I came to the Netherlands in 2009 for my master study in applied physics in the pursuit of my dream to be a good physicist. Most of my time are related to Optica. With this PhD thesis, I will say good bye to the Optica group after so many years. I would like to thank all the friends, colleagues and students for your company through this journey.

First of all, I would like to thank all my teachers that lead me to the world of science. Sharing knowledge with young generations and preparing them a sound basis to create is why universities exist. The example set by many of my great teachers is one of the motivations that encourage me to pursue this PhD.

I would like to thank Paul for giving the opportunity to perform my PhD study in Delft. Paul has been always great in teaching physics and his devotion to this has inspired me since I was a master student. After so many years working with Paul, I learned much more about academia, sometimes by observing him as the role of the head of Optica, promotor, grant writer, funding lobbyist and his roles in regional and international co-operations. I don't know how he manages this insanely busy job and definitely couldn't imagine this before I decided to pursue a PhD and a career in academia. I am grateful for his efforts in giving me the luxury environment and freedom to perform pure research and grow as an independent researcher.

Life isn't easy as a PhD candidate. I am so lucky to have Nandini as my daily supervisor and a friend to guide and encourage me through this whole process. She listens to my difficulties, worries and complains. I am grateful for her confidence in us students and all her support. I sometimes feel that she trusts her students more than we trust ourselves, and that is very important, especially when you sometimes spent weeks in the cleanroom developing recipes. The positiveness and empathy that I learned from her will always stay with me and as a 'karma' I shall expect a lot of empathy from me to others as a return.

Special thanks need to be given to dr. Zheng Xi. The scientific discussions we had were truly inspirational and fruitful. His hard working and senses about Physics is incredible and I fully believe he will have a great research career. Most of my works related to nano-antennas are supported by the numerical software Cyclops3D. I am grateful for its creators, especially Arthur Wachtters, though we haven't met yet, for his helps through our email exchange which is even faster than my colleagues. I would like to thank Google to translate and Sander for double check my dutch version of the summary of this thesis.

I would like to thank Pieter de Bokx for his involvement in this project. As a chemist by training, he has tried very hard to understand the physics and help define the project from the very beginning. I am very grateful for his arrangement for the experimental facilities in Eindhoven, as well as to Emile, Thim and Rob for their helps in making the setup. I would also thank Gopika and Nishant for introducing me to the cleanroom and the cleanroom staffs for their daily supports.

Apart from the researches in this thesis, I have got the opportunity to get involved in other projects and collaborate with many talented researchers including Sander, Jorn, Yuchen, Xueming, Sarathi, Nitish, Jonas, Jianrong Gao, Rob Remis, etc. I would like to thank them for the discussions we had and what I learned from them.

My research career starts from Optica, I am proud of it when we do well and promote good science and I am sad if we demotivate ourselves. Optica is 70 years as a research group in 2017 and I hope it keep training young talents and generating good scientific results. But it is much more than just research. I stay in Optica for so long that I always consider it as my family in the Netherlands and so many faces pop up as I write. I would like to thank my colleagues and friends who come from all over the world and shared the 'gezelligheid' in our Optica group, for the memorable coffee breaks (maybe too long and too often...), uitjes, lunches, potlucks, films, agoras, Xmas dinners, graduation parties etc... I would like to thank Yvonne, Thim, Roland and Chris for their supports, Peter for his sharing of Jazz and his contributions to every graduation songs, my office mate Luca, Katsiaryna, Matthias and Sander, my Indian friends Nitish and Gopika (you two are my example of perfect couple, enjoy your life ahead), Sarathi, Nishant, Gopa and Priya, my Mexican friend Adonis, Tania, Victor and Aura, the Germans who don't drink beer Andreas, Thomas, Daniel and Matthias, Alessandro the Italian bartender, Daniel, Luiz, Edgar, Alberto, Diego and Fellipe from the south hemisphere, Joseph, Omar, Jeff, Paul Planken, Peter, Sven for their scientific discussions, Aurele, Man, Mounir, Hamed, Silvania, Anna, Marco, Nick, Ruben, Liesbeth, Gyllion, Milena, Borys, Mahsa as well as my small Chinese society Ying, Yifeng, Zhe, Zheng Xi, Chengliang, Fanhe, Yuchen, Zheng Zhu, Peiwen, Xiaosi, Xukang, Zhongwen, Kefei. Please forgive me, if I missed you.

Last but not least, I would like to thank my family, especially my parents and my wife Shan, for their endless love and support.

CURRICULUM VITÆ

Lei WEI

EDUCATION

- 2002–2005 High School
Taihe No. 1 High School, Taihe
- 2005–2009 Bachelor of Science in Optical Information Science and Technology
University of Electronic Science and Technology of China, Chengdu
- 2009–2012 Master of Science, ir. in Applied Physics
Delft University of Technology, Delft
Thesis: Evaluation and Application of Extended Nijboer
Zernike theory for Optical System Design
Supervisor: Prof.dr. H.P. Urbach(TU Delft) and Dr. Bernd Klee-
mann(Carl Zeiss AG, Oberkochen)
- 2012–2017 PhD candidate, Optics
Delft University of Technology, Delft
Thesis: Scattering control of optical nano-antennas with designed exci-
tations
Supervisor: Prof.dr. H.P. Urbach and Dr. Nandini Bhattacharya

AWARDS

- 2005–2009 Scholarship for Undergraduate study, UESTC
- 2009 Graduate with distinction, UESTC
- 2009–2011 Full Scholarship from Faculty of Applied Science, TU Delft
- 2012 ir. cum laude/ Msc with distinction, TU Delft

LIST OF PUBLICATIONS

1. **L. Wei**, N. Bhattacharya and H.P. Urbach, *Adding a spin to Kerker's condition: angular tuning of directional scattering with designed excitation*, *Optics Letters*, **42**, 1776 (2017).
2. B. Mirzaei, J.R.G. Silva, Y.C. Luo, X.X. Liu, **L. Wei**, D.J. Hayton, J.R. Gao and C. Groppi, *Efficiency of multi-beam Fourier phase grating at 1.4 THz*, *Optics Express*, **6**, 6581(2017).
3. Z. Xi, **L. Wei**, A.J.L. Adam, H.P. Urbach and L. Du, *Accurate Feeding of Nanoantenna by Singular Optics for Nanoscale Translational and Rotational Displacement Sensing*, *Phys. Rev. Lett.*, **117**, 113903 (2016).
4. **L. Wei**, Z.Xi, N. Bhattacharya and H.P. Urbach, *Excitation of the radiationless anapole mode*, *Optica*, **3**, 799 (2016).
5. J. Zimmerling, **L. Wei**, H.P. Urbach and R. Remis, *A Lanczos model-order reduction technique to efficiently simulate electromagnetic wave propagation in dispersive media*, *J. Computational Physics*, **315**, 348(2016).
6. **L. Wei** and H.P. Urbach, *Shaping the focal field of radially/azimuthally polarized phase vortex with Zernike polynomials*, *J. Optics*, **18**, 065608(2016).
7. J. Zimmerling, **L. Wei**, H.P. Urbach and R. Remis, *Efficient computation of the spontaneous decay rate of arbitrarily shaped 3D nanosized resonators: a Krylov model-order reduction approach*, *Applied Physics A*, **122**, 1(2016).
8. X. Li, **L. Wei**, R.H. Poelma, S. Vollebregt, J. Wei, H.P. Urbach, P.M. Sarro and G.Q. Zhang, *Stretchable Binary Fresnel Lens for Focus Tuning*, *Scientific Reports*, **6**, 25348(2016);
9. Z. Xi, **L. Wei**, A.J.L. Adam and H.P. Urbach, *Broadband active tuning of unidirectional scattering from nanoantenna using combined radially and azimuthally polarized beams*, *Optics Letters*, **41**, 33(2016).
10. S. Roy, M. Bouwens, **L. Wei**, S.F. Pereira, H.P. Urbach and P. van der Walle, *High speed low power optical detection of sub-wavelength scatterer*, *Rev. of Sci. Inst.*, **86**, 123111(2016).
11. A.P. Konijnenberg, **L. Wei**, N. Kumar, L. Couto Correa Pinto Filho, L. Cisotto, S.F. Pereira and H.P. Urbach, *Demonstration of an optimized focal field with long focal depth and high transmission obtained with the Extended Nijboer-Zernike theory*, *Optics Express*, **22**, 311(2014);